Redistribution of sidechain-sidechain interactions govern ligand-specific binding affinity changes in missense Shank1 PDZ mutants

Authors

Anna Sánta[1], Zsófia E. Kálmán[1], Eszter Nagy-Kanta[1], Zoltán Gáspári[1], Bálint Péterfia[1*]

[1]Faculty of Information Technology and Bionics, Pázmány Péter Catholic University, Budapest, Hungary

***Corresponding author:**
Name: Bálint Péterfia
Address: Práter utca 50/A, 1083 Budapest, Hungary
Telephone: +36 (1) 8864 739
Email: peterfia.balint.ferenc@itk.ppke.hu

Running title

Ligand binding in Shank1 PDZ missense mutants

List of content

28 manuscript pages; 2 supplementary files: 8 pages of supplementary figures and 15 tabs of supplementary tables; 2 tables, 7 figures

Supplementary files

Three supplementary files are provided. SupplementaryFigures.pdf contains the full series of schematic representations of ligand binding (Fig. S1, pages 1-6), a series of figures depicting PCA modes that provide better visibility of some data (Fig. S2, page 7), a series of figures showing H735 dihedral distributions (Fig. S3, pages 8-10) and an original SDS-PAGE image (Fig. S4, page 11). SupplementaryTables.xls contains a detailed list of protein constructs used for experiments (S1), experimental data (S2-S4), comparison of docked complex models to experimental and AlphaFold structures (S5), an alternative version of the figure summarizing MD results (Fig. 4B) which contains numerical data and additional columns for better accessibility (S6), tables containing H735 X_1-X_2 dihedral angles throughout the simulations (S7-S9) and PCA data (S10). Finally, SupplemetaryPDBs.zip contains 90 PDB ensemble files, each containing 500 MD simulation snapshots.

Abstract

Shank proteins represent a family of abundant scaffolds in the postsynaptic density. Their dysfunctions had been identified as possible causes behind autism spectrum disorders and various types of cancer. The remarkably promiscuous PDZ domain of the Shank family is highly conserved through isoforms, and contains a unique dynamic segment, the β2-β3 loop, which is likely to play an important role in ligand selectivity. We used the Shank1 PDZ as a model system to analyze the perturbing effects of five disease-associated missense mutations on the binding of different partner peptides. Using experimental methods and molecular dynamics simulations, we characterized the interactions in detail, focusing on their dynamic aspect. While the investigated mutations in general weaken most interactions, the R736Q mutant, unique in having increased thermal stability, also binds the GKAP peptide with higher affinity than the wild type. Overall, our results show that the perturbing effect of mutations is highly partner-specific and depends on the dynamic rearrangements of both uniformly occurring and ligand-specific residue-residue interactions.

Statement

The Shank1 protein plays a possible role in autism spectrum disorders and also cancer, two conditions that affect many lives. Our paper provides a more-detailed-than-ever model of Shank1 PDZ - including disease-associated mutants - bound to its ligands, and we highlight the importance of flexibility and dynamics, which appear to be the main driving force behind its ligand selectivity, and reveal remarkable complexity hiding within this small protein domain.

Keywords (6): Postsynaptic density; PDZ domain; peptide binding; loop dynamics; missense mutation; MD simulation

Abbreviations

ASD: autism spectrum disorder; BLI: biolayer interferometry; CD: circular dichroism; FP: fluorescence polarization; FT: flowthrough; GST: glutathione S-transferase; IEC: ion exchange chromatography; IMAC: immobilized metal ion chromatography; KI: knock-in; KO: knock-out; MD: molecular dynamics; PCA: principal component analysis; PD: phosphate buffer; PDZ: PSD-95, DLG1, ZO-1 domain; PSD: postsynaptic density; RT: room temperature; SEC: size exchange chromatography; TM: melting temperature; TSA: thermal shift assay

Introduction

Shank1, member of the Shank family consisting of three proteins, is one of the major scaffolding proteins at the postsynaptic density (PSD) of excitatory synapses composed of ankyrin-repeat-, SH3-, PDZ- and SAM domains as well as a long, proline-rich disordered region. (Sheng & Kim, 2000) ***(Fig. 1A)*** Due to these protein interacting domains and regions, Shank1 is able to form supramolecular complexes with a great number of other proteins. Shank1 has been associated with neurological disorders such as autism spectrum disorder, schizophrenia, mental disability and recently, its role in tumor progression has also been revealed. The PDZ domain of Shank1 is a remarkably promiscuous Class I PDZ domain, with a unique b1-b2 loop region that is only found in the Shank family. Otherwise, its secondary structure composition is highly conserved, as well as its regions involved in partner binding. Structural features of its bound state are well documented via experimentally determined structures, with several binding partners, especially GKAP. (Ali et al., 2021; Im et al., 2010, 2003; J. H. Lee, Park, Park, Kim, & Eom, 2011; Ponna et al., 2018; Zeng et al., 2016) ***(Fig. 1B, 1C, 1D)***

Regarding neural disorders, unlike Shank2 or -3, Shank1 is known to be expressed predominantly in the brain, in a distinctly different pattern with highest abundance in the cortex, cerebellum and hippocampus. Shank1 knockout mice exhibit a complex behavioral phenotype and decreased expression of GKAP and Homer proteins, which are well-known direct interaction partners of Shank1. The C terminus of GKAP is bound to the PDZ domain of Shank1, while Homer interacts with the Proline-rich segment. So far, Shank1 have been regarded as a low risk ASD gene probably due to the obscure, mild phenotype of KO mice - unlike Shank3, which is associated with severe autism-like symptoms in KO mouse models, and is the cause of Phelan-McDermid syndrome in humans. Lack of Shank3 results in downregulation of the Akt/mTORC1 pathway, resulting in decreased protein synthesis and neuronal dysfunction. (Burbach, 2016) However, recently, knock-in mice bearing the R882H missense mutation (localized downstream to the PDZ domain) have been reported to display core ASD symptoms with social disability and repetitive behaviors due to downregulation of mGluR1-Homer-IP3R1-calcium signaling. (Qin et al., 2022) This finding underlines that missense mutations are promising tools to explore the role that Shank proteins and their domains play in neural disorders. This suggests that loss-of PDZ domain missense mutations could be used to elucidate the role of the GKAP-Shank1 interaction (and other PDZ interactions) in neurological disorders. Only one missense mutation of the Shank1 PDZ domain (R736Q) is described in relation to ASD, but its pathogenicity is uncertain. (Leblond et al., 2014)

Beyond their synaptic functions, Shank proteins have been recognized to play a role in several malignancies with altered expression and survival correlation. (Chang et al., 2022; Lilja et al., 2017; Xu et al., 2021) Shank expression or DNA methylation are independent prognostic markers in colon cancer and leukemia. (Loi et al., 2019; Wang, Lv, & Liu, 2020) In addition, the expression of Shank proteins regulates the fate and development of stem cells through different signaling pathways. (Liu, Yuan, Lau, & Li, 2022) The tumor promoting effects of Shank1 were found to be mediated by the AKT/mTOR signaling pathway in colon cancer cell lines, and by MDM2 in non-small lung cancer cells. (Chen et al., 2022; Wang et al., 2020) Nuclear translocation of MDM2 is known to be triggered by the AKT/mTOR pathway, which suggests a common pathway of Shank1 in these cell lines. There is no direct evidence as to which domain of Shank1 may play a role in activating the Akt/mTOR pathway.

Deletion of the PDZ domain causes Shank2 to lose its oncogenicity via Hippo signaling, but whether Shank1 or Shank3 also participate in this pathway is unknown. The aforementioned Shank2 pathway is driven by the interaction with ARHGEF7 (βPIX), also a known interaction partner of the Shank1 PDZ. (Xu et al., 2021)

As of now, no mouse model is known that was created with the aim of modeling oncogenic behavior of Shank1 specifically. Xenograft experiments with overexpressed Shank1 and Shank2 showed tumor promoting effects. (Chen et al., 2022; Xu et al., 2021) No specific point mutations of Shank1 are known to be directly associated with cancer. However, several point mutations found in tumor samples are documented in the COSMIC database. (Sondka et al., 2024) ***(Fig. 1E)***

To avoid investing significant effort in generating transgenic mice with neutral benign point mutations, it is crucial to experimentally characterize potential variants in vitro. This study examines the effects of one ASD-associated and four somatic missense variants of the Shank1 PDZ domain on partner binding capacity and structure in vitro, starting with GKAP as the reference model, and expanding to four other partners with possible clinical significance. From these additional partners, βPIX bears a C-terminal binding motif, whereas ARAP3, ATG13 and mTOR exhibit internal binding sequences. We assess the thermal stability and binding properties of the Shank1 PDZ mutants and use molecular dynamics simulations to aid the interpretation of our findings.

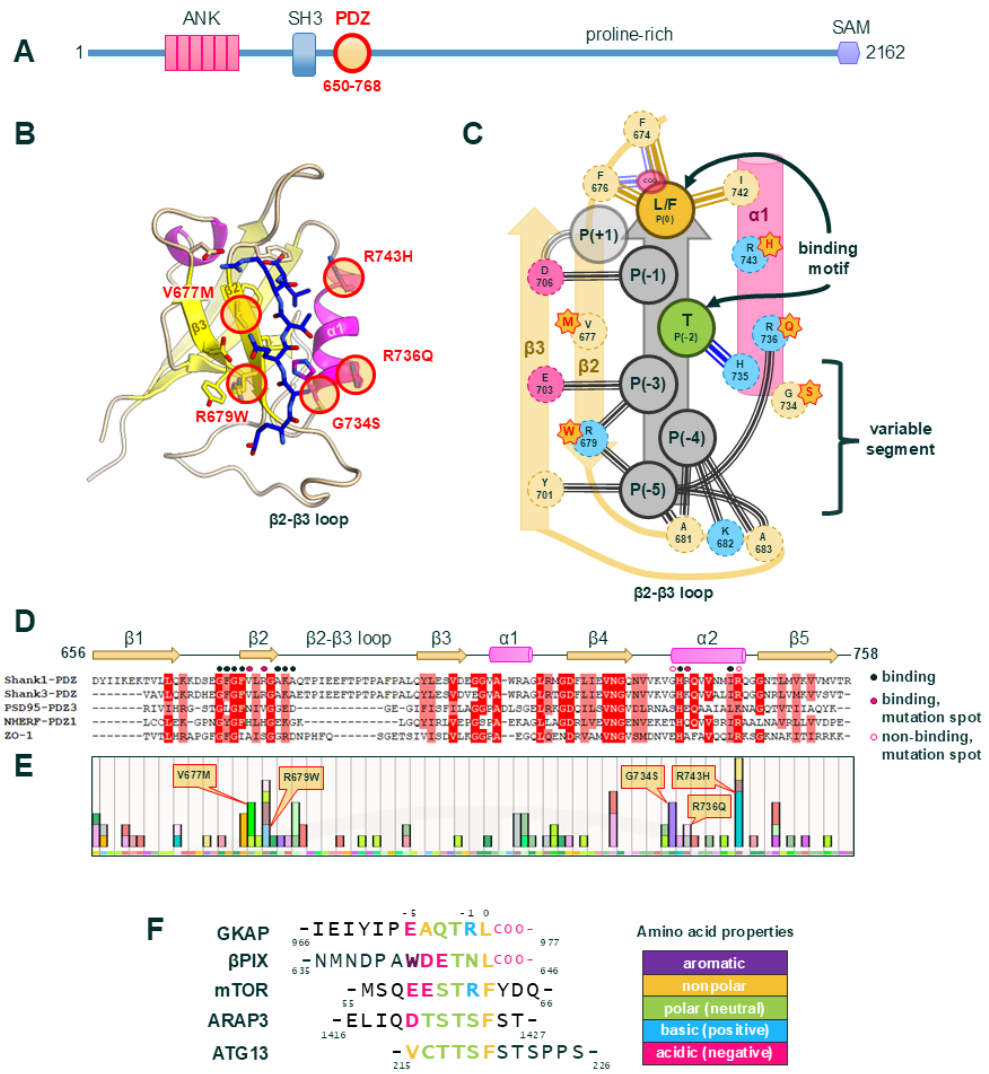

Figure 1. The Shank1 PDZ and its binding modes. (A) Domain composition of the Shank1 protein, with the PDZ domain and the span of our construct highlighted in red (the canonical PDZ spans from 663-757). For a list of constructs, refer to the Supplementary Tables. **(B)** Structure model of the Shank1 PDZ, bound to the C-terminal of GKAP (blue), based on PDB ID 1Q3P. Secondary structure elements are colored yellow for beta-strands and magenta for alpha-helices. Locations of point mutations are circled red and labelled. **(C)** Schematic representation of the Shank1 PDZ ligand binding pocket, with variable sidechain bonds depicted with black triple lines. Note that not all of the variable bonds are present in all peptide binding interactions. The nonpolar interactions of P(0) and the hydrogen bond of P(-2) are highly conserved. The carboxylate interaction is only relevant in terminal motifs, while P(+1) is only found in internal motifs, therefore they are depicted in lower opacity to reflect that. **(D)** Secondary structure composition of the Shank1 PDZ, with multiple sequence alignment comparing it to other PDZ domains. Identities and similarities within 80% are highlighted with red and light red respectively. Note that the β2-β3 loop segment is only found in the Shank PDZ

domains. Positions that participate in binding according to currently known experimental structures of the Shank1 PDZ and/or are affected by mutations are marked, with legend included. **(E)** Histogram of mutations from the COSMIC database, overlaid onto the Shank1 PDZ sequence. The mutations analyzed in this study are labelled. **(F)** Partner peptides analyzed in this study, with binding motif amino acids colored according to their properties.

Results

The most frequent somatic and ASD-associated mutations affect positions around the ligand-binding pocket

Somatic mutations for this study were picked from the COSMIC database, originally with the intent of preferring binding-site mutations for experimental investigation. Crystal structures 1Q3P, 3QJN (and 3L4F), 7A9B, 6YWZ and 8S1R (which display Shank1 PDZ in complex with GKAP, βPIX, ARAP3, a modified synthetic construct based on GKAP, and a synthetic peptide with sequence similarity to mTOR, respectively) were used as references to analyze the context of each mutation. (Ali et al., 2021; Hegedüs et al., 2021; Im et al., 2010, 2003; J. H. Lee et al., 2011; Li et al., 2024) First, it was noted that the binding site is indeed a hot spot for mutations, and the most common missense mutation spots were located on either the β2 strand or the α2 helix forming its main parts. Four mutations fitting this criteria were picked. The one mutation picked from a study on ASD is also located in this area and has two entries in COSMIC. ***(Fig. 1E)*** (Leblond et al., 2014; Sondka et al., 2024)

The most common mutation according to the COSMIC database, R743H, is documented to interact only in some structures. In its close proximity, the C-terminal residue P(0) of the ligand is buried within a hydrophobic pocket formed by F674, F676 and I742, which is partially covered by R743, which simultaneously also might form a salt bridge with the peptide backbone at P(-1), however this was only observed in some models. (Ali et al., 2021; J. H. Lee et al., 2011) We predict that a mutation to histidine, a sidechain with less charge and volume, could unfavourably affect these interactions. Another possibility is a transient interaction which was seen only in the study about 6YWZ, the structure containing a synthetic GKAP-based ligand, so far. This interaction involves an acylhydrazone fragment component at the same position as P(-5), for which, R743 competes with R736 and R679. (Hegedüs et al., 2021)

Residues 677 and 679 are both on the β2 strand, and both bear side chains that were either documented to interact with ligands, or are in close proximity to a known interaction. V677 in the WT is surrounded by P(-1) and P(-3) of the ligand, both of which are possibly part of the binding interface in most of the complexes. Ligand positions P(-3) and P(-5) form various interactions with R679 in all known structures, including the aforementioned dynamic, transient interaction with the synthetic, GKAP-based ligand. (Ali et al., 2021; Hegedüs et al., 2021; Im et al., 2003; J. H. Lee et al., 2011; Li et al., 2024; Ponna et al., 2018) These two mutations are the closest to the β2-β3 loop in the sequence, a highly

mobile segment unique to and conserved in Shank PDZ domains. (J. H. Lee et al., 2011)

The G734S mutation is located right before the α2 helix. It is in similarly close spatial proximity to the β2-β2 loop as position 679, and is next to residue H735 which H-bonds to the conserved Thr P(-2). (Im et al., 2003)

R736Q is unique among the mutations in this study as the only one that was known to be associated with ASD, although entries are also documented in the COSMIC database. (Leblond et al., 2014; Sondka et al., 2024) The sidechain is on the surface and there is no data supporting that it contributes to any binding interactions with known partner proteins, although it was observed to interact with the aforementioned synthetic ligand based on the GKAP peptide, along with R743 and R679. (Hegedüs et al., 2021)

Missense mutations affect the stability but not the structure of Shank1 PDZ

ECD spectra recorded at 30 °C suggested a well folded, globular structure with beta sheet predominance that is in accordance with the available X-ray structure of the domain (PDB ID 1Q3O (Im et al., 2003)) and PDZ domains in general. No significant changes in the ECD spectrum at 30 °C were observed in any of the mutated structures. ***(Fig. 2A)*** However, remarkable differences were detected in their thermal stability both by thermal shift assays (TSA) and CD scan measurements. ***(Fig. 2B, 2C, Table S2)*** Melting points observed by TSA were found to be 59 °C for the WT, and 56.9, 52.0, 58.2, 61.6 and 58.8 °C for the V677M, R679W, G734S, R736G and R743H mutants, respectively. ***(Fig. 2B, 2C)*** These are in good accordance with the CD scan measurements. ***(Table S2, S3)*** Both the decrease at 200 nm and the increase at 210 nm in the CD signals by the heating suggests the increase of the proportions of random coil and beta structural elements in the domain.

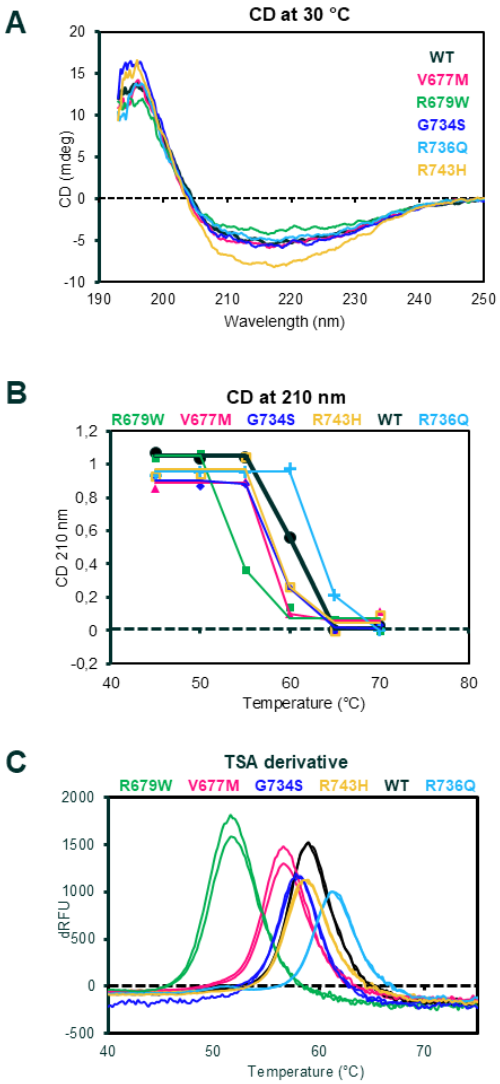

Figure 2. Structural stability of the Shank1-PDZ point mutants. (A) CD values at 30°C. Note that the curves are nearly identical. **(B)** Normalized CD curves of the PDZ isoforms at 210 nm. Note that the inflection points of the curves align with the peaks in the TSA data below, indicating that the results from the two methods are consistent. **(C)** Thermal shift assay results of the different Shank1 PDZ isoforms. Peaks indicate melting points.

Effect of the mutations on domain stability and GKAP binding move in parallel

In order to examine the functional effect of the mutations, interaction of the wild type and mutant PDZ domains with the GKAP C terminal GH1 construct was tested by a simple pull-down assay. ***(Fig. 3A)*** The R679W variant was pulled down in significantly less amount by GH1 bait than the other variants, for which these experiments showed little difference relative to the wild type. This result was corroborated by fluorescence polarization spectroscopy measurements. Using a 12 amino acid long, FITC labeled GKAP C terminus peptide ligand (Ct12), the dissociation constants (K_d) of WT, V677M, R679W, G734S, R736Q and R743H mutants was calculated to be 5.4, 13.5, 59.7, 8.4, 2.9 and 6.7 μM respectively, indicating a more than tenfold difference between the affinity of the WT and the R679W variant. ***(Fig. 3B, Table S4)*** Highly similar ratios were obtained by biolayer interferometry, although with slightly lower measured K_d values, 1.5 and 14.5 μM for WT and R679W respectively. ***(Fig. 3C, Table S4)*** Taking the results of all methods into account, it can be stated that variants R679W and V677M attenuate the interaction with GKAP protein to a notable extent. ***(Table 1)***

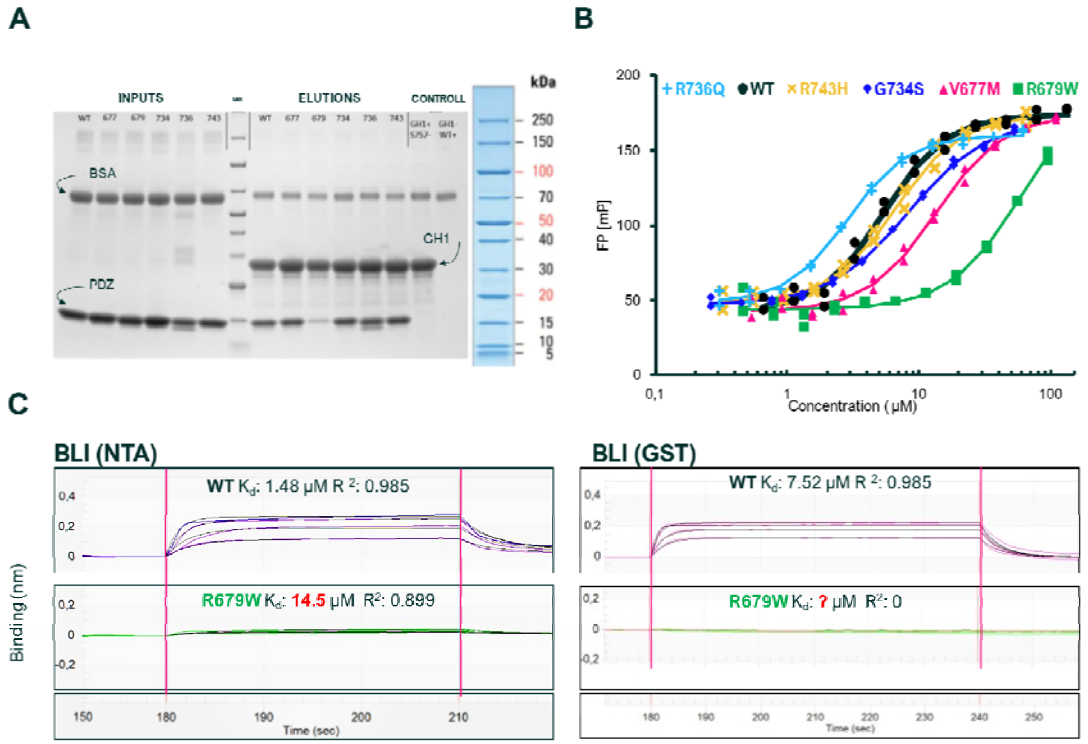

Figure 3. Interaction results with the GKAP partner protein. (A) SDS-PAGE of the pull-down assay which allowed for quantitative measurement of relative binding affinities.**(B)** FP results with fitted curves

for all mutants. **(C)** Examples of BLI datasets with fitted curves and resulting K_d values and R2 values describing fitting quality. Note the similarities in curve kinetics and biolayer thickness in the respective experiments.

Remarkably, the ligand binding ability of Shank1 PDZ domain moves in parallel with the effect of the mutations on the stability: the V677M and R679W mutants both exhibit a weaker interaction and a lower T_m than the WT domain, whereas the R736Q variant forms a slightly stronger interaction and has a higher T_m. ***(Fig. 4A)***

	ΔAUC (gel) (%)		**K_d (FP) (μM)**		**K_d (BLI-NTA) (μM)**		**K_d (BLI-GST) (μM)**	
WT	21	***1***	5.4	***1***	1.5	***1***	7.52	***1***
V677M	37	***1.8***	13.5	***2.5***	6.7	***4.5***	62.6	***8.3***
R679W	84	***4***	59.7	***11.1***	14.5	***9.7***	NA	***NA***
G734S	47	***2.2***	8.4	***1.6***	1.7	***1.1***	52.4	***7.0***
R736Q	16	***0.8***	2.9	***0.5***	2	***1.3***	1.79	***0.2***
R743H	25	***1.2***	6.7	***1.2***	1.4	***0.9***	27.3	***3.6***

Table 1. Summary of all binding affinity data obtained with Shank1-PDZ mutants and GKAP. Relative binding affinities are listed next to each data column in bold italic.

Binding affinity changes of the weaker binders exhibit varying correlations with domain stability

In order to investigate the partner binding of Shank1 PDZ mutants with other partners, we established a BLI-based protocol using GST-tagged peptides. First, we confirmed that the GST-GKAP-CT12 construct produced similar K_d values to those obtained with FP and NTA-BLI as described above. ***(Table 1, Table S4)*** We observed the very same trends but the absolute K_d values appear to be higher than the NTA-BLI results, leading to amplified differences between the variants. As a result, the most unstable mutant, R679W did not produce measurable binding with any of the peptides, therefore no K_d values were obtained for it. For all peptides, the relative K_d values with respect to the WT domain agree well with those reported by Ali et al., with a correlation coefficient of 0.99, but the absolute values are tenfold higher. ***(Table 2)*** We conclude that regardless of these discrepancies stemming from the different methodologies, the relative values within our model system were retained and therefore relevant.

All the peptides turned out to be weaker binders to the wild type PDZ than GKAP, in the following order: βPIX (23.23 uM), ARAP3 (35.76 uM), ATG13 (39.15 uM) and mTOR (720 uM), with the last being significantly, over one order of magnitude weaker than the others. The strongest binder after GKAP is βPIX, the only other C-terminal peptide. Generally, the destabilizing mutations exerted a destabilizing effect on the interactions, with the mutants V677M, G734S and R743H consistently producing higher K_d values than WT in all experiments. However, the different mutations affected the binding of the peptides in a highly variable manner. For example, R743H, which binds GKAP only slightly weaker than the WT variant, was shown to be the second weakest binder to βPIX after V677M, and produced similar results to V677M and G734S for the ARAP3 interaction. Even more intriguing are the results with R736Q, the mutant with the highest thermal stability and GKAP-binding affinity: for most peptides the R736Q variant is a weaker binder than the WT, and even with ATG13 it was merely on par with WT. In summary, the correlation observed between thermal stability and GKAP-binding did not apply to any other of the investigated peptides. Overall, the trends indicate that higher destabilization is accompanied by weaker binding, but there is considerable variability between the ligands. ***(Fig. 4A)***

	K_d (ITC) (Zeng et al., 2016) (μM)	K_d (ITC) (Im et al., 2010) (μM)	K_d (MST. FP) (Ali et al., 2021) (μM)	K_d BLI-GST) (μM)	K_d (ITC) (μM)
GKAP	5.81			7.52	0.45
βPIX		2.6	0.79	23.23	
ARAP3			*3.65	35.76	
ATG13			3.8	39.15	
mTOR			84	*812.5	

*value averaged from two different results obtained by same group each

Table 2. Summary of K_d values with various peptides and WT Shank1-PDZ.

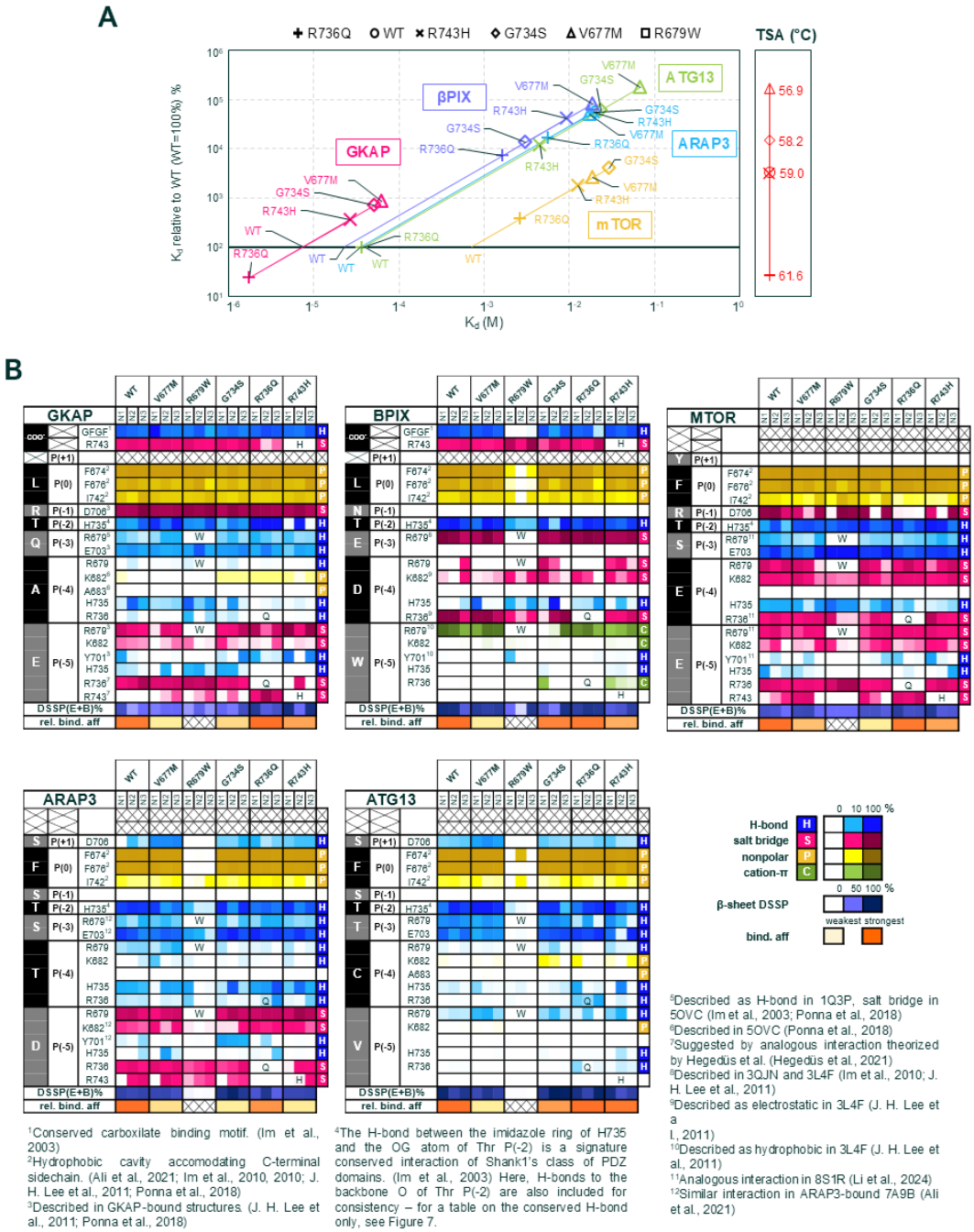

Figure 4. Interactions with βPIX, mTOR, ARAP3 and ATG13. (A) Relative and absolute K_d values of all mutants and peptides. For a table of full series of values, refer to the Supplementary Tables. **(B)** Tables representing all PDZ sidechain to peptide sidechain/backbone interactions in our models. Specific interactions were given footnotes listing related literature. For a full summary of exact values refer to the Supplementary Material.

Docking calculations accurately reproduce available experimental structures with wild-type Shank1 PDZ

To rationalize the peptide-specific changes in the interactions with the mutant Shank1 PDZ variants, we performed computational modeling of the PDZ:peptide complexes. Docking simulations were performed and it was determined that those models which have corresponding experimental structures available in the PDB (the GKAP, βPIX and ARAP3 complexes) reproduced the peptide backbone conformations and sidechain orientations observable in said structures. ***(Table S5)*** However, these models were not suitable for detailed sidechain-sidechain interaction analysis, due to the incomplete side chains in the docking output necessitating repair steps which could potentially distort their conformations. Moreover, structural dynamics are known to play an important role in the Shank1 PDZ, which is not incorporated into these static models.

MD simulations provide a good approximation of experimentally determined stability

To analyze the PDZ:peptide interactions in more detail, MD simulations were performed on all mutant-peptide combinations, using the models created with docking as the starting point. All complexes remained stable during the simulations, with no significant changes in the overall fold of the PDZ domain, with partial peptide dissociation only occurring for some R679W complexes, which is in agreement with the experimental results suggesting it to be the weakest binder. Secondary structure elements as assessed by DSSP remained highly similar to known Shank1 PDZ structures. The peptides exhibited a varying degree of β-strand propensity and low mobility at their conserved P(0)-P(-2) segment and increased dynamics towards the N-terminals. Next, to analyze the PDZ:ligand bond network, we extracted the interactions of the PDZ side chains to peptide side chains and backbone, and omitted references to backbone-backbone interactions, (except in unique cases), as the presence of a backbone-backbone H-bond network in the extended β-sheet binding mode is trivial, and is also redundantly represented by β-strand DSSP annotations. ***(Fig. 4B, Table S6)***

The β2-β3 loop explores different conformations in the complexes

The long, flexible β2-β3 loop is unique to the Shank PDZ domains, and it explored a large conformational space during our simulations. NMR chemical shifts indicated the presence of a short helical segment in the free domain (Sánta et al., 2022), and our DSSP analysis of the MD trajectories reveals that this region shows variable helical/turn character, usually below 50%. No discernible pattern was noted in the helical propensity of different complexes and mutants. ***(Fig. 5A)***

The loop is relatively far from the mutated sites and remains generally flexible in all complexes. However, principal component analysis reveals some interesting differences between the PDZ variants. Here we focus on those that can be regarded as the most robust ones when taking into account all simulations performed.

The first two principal components are dominated by a shorter region of the loop (approximately 681-690), the first mode corresponding to a motion within the plane of the β-strand formed by the ligand but perpendicular to its long axis. The second mode is largely perpendicular to the first, with the loop alternating between being below and above the plane of the ligand strand. The third PC can be best described as a "compaction-extension" motion of the whole loop. ***(Fig. 5B)***

Interestingly, mode 1 exhibits a largely bimodal distribution, with two clusters and a sparsely sampled transition region between them. When considering all our simulations, most peptides and mutants populate both clusters, although individual simulations might get stuck in one of them. As for mode 2, the full range of this mode is only explored by the βPIX complexes of different PDZ variants, with the wild type and the R679W exploring the two extremes. For the complexes with this peptide, the conformational space covered by the WT domain is well separated from that characteristic for the mutants. For all other peptides, including GKAP, the general pattern is that the wild type complex exhibits the highest flexibility and the mutants reduced mobility, the extent of which can highly vary. As it is not expected that our simulations exhaustively cover all relevant conformational states, we refrain from more specific statements here but note that our simulations suggest that the behavior of the β2-β3 loop is not entirely independent of neither the mutation nor the bound peptide.

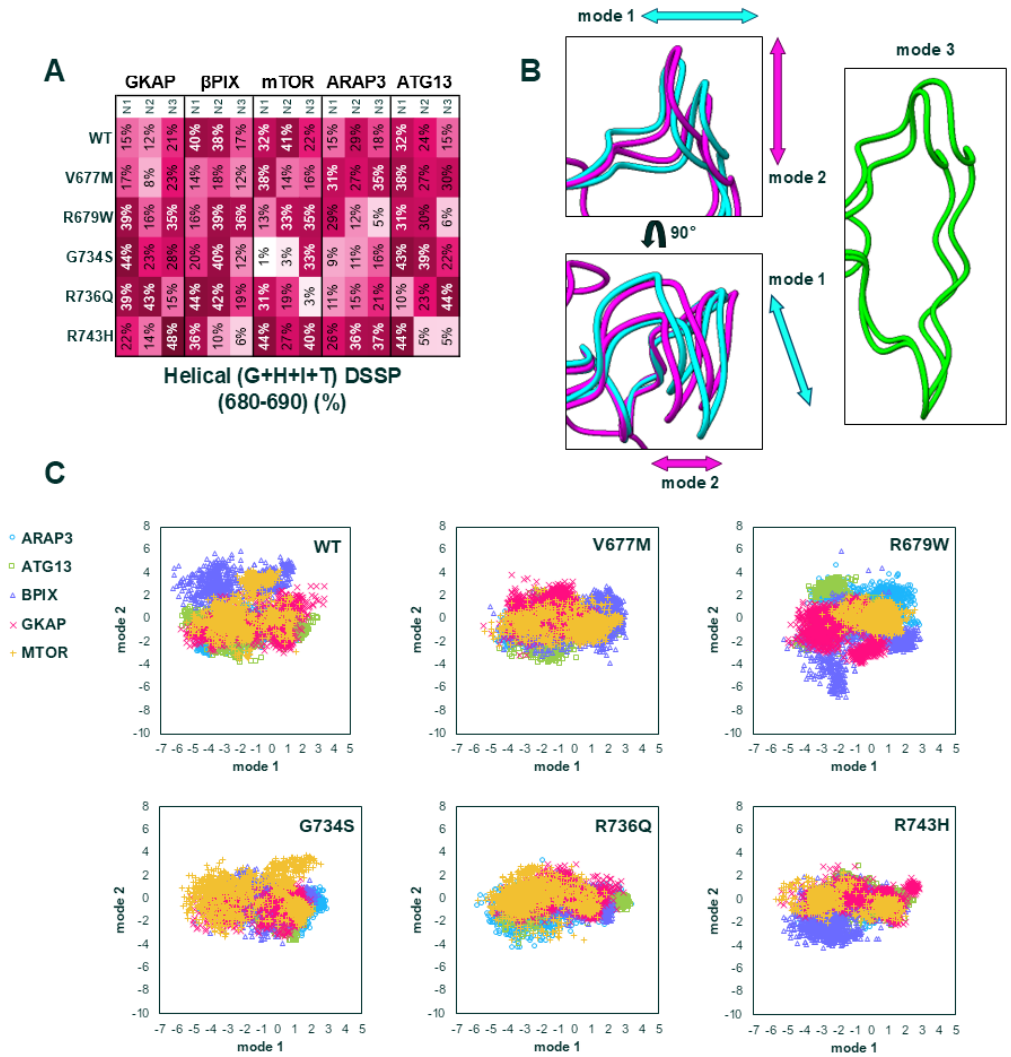

Figure 5. Dynamic properties of the βB-βC loop. (A) Summary table showing the presence of helical DSSP annotations (G, H, I, T) throughout MD simulations as percentage, on the 680-690 segment (βB-βC loop, mobile segment), with proportional color intensity. **(B)** Backbone models representing the first three PCA modes. Note that the amplitude pictured was arbitrarily chosen for representative purposes and does not show the actual extent of loop mobility. **(C)** PCA modes 1 and 2 of the βB-βC loop, separated by mutant, colored by peptide. A series of reversed figures (ie. separated by peptide) is provided in the Supplementary Material.

A novel role of R743 in carboxylate binding of the C-terminal motifs in GKAP and βPIX

The main-chain carboxyl group of the C-terminal peptides GKAP and βPIX was expected to form a firm hydrogen bond with the conserved carboxylate binding 673-GFGF-676 motif of the PDZ domain. However, an alternative conformation emerged in our models, where the terminal carboxyl group flips and forms a salt bridge with R743. This observation suggests a novel, important role of the R743 sidechain besides being part of the "arginine triad" capable of binding P(-5), and hydrophobic stacking. The alternative carboxylate-stabilizing interaction of the R743 sidechain was not considered as an important factor in previous known models of the Shank1 PDZ, which made the abundance of the R743H mutation in tumor samples rather elusive. The carboxylate-binding role offers an explanation to this, as well as the weaker binding affinity, since the observed frequency of interactions of the carboxylate was the lowest in the R743H mutant, as H743 does not form this interaction. A notable difference between the two C-terminal peptides analyzed was that while in the GKAP complex, each mutant exhibited both C-terminal carboxylate interactions, the βPIX peptide in complex with the R679W mutant consistently showed an almost exclusive preference for the R743 salt bridge. ***(Fig. 4B)***

The Shank1:GKAP complex: alternate interactions of H735 and P(-5) Glu in the WT and altered dynamics in the mutants

Molecular dynamics simulations on the WT domain with the GKAP peptide reproduce most of the previously described residue:residue interactions. PDZ residues F674-F676-L678-I742 form a hydrophobic pocket accommodating P(0) throughout the simulation. Residue D706 forms a characteristic end-on bidentate salt bridge with the P(-1) Arg in ~80% of the simulation frames. However, the expected P(-3) Gln or P(-5) Glu interactions with R679, especially the former, appear relatively weak, so does the P(-3):E703 interaction, and the P(-5):Y701 bond barely even form in two out of three simulation runs. Remarkably, P(-5) Glu forms alternate interactions with R736, which results in a bent conformation of the peptide that results in the P(-4) and P(-5) backbones facing H735, who in turn forms transient H-bonds to these positions, while also dynamically changing its side chain orientation to bind to P(-2) Thr. The latter should be its expected conformation characteristic of Class I PDZ domains, however in our simulations its frequency is remarkably low (an average ~30%) due to the competition with the alternative P(-4)-P(-5) bonds. ***(Fig. 4B)***

In the mutants, the hydrophobic P(0) interaction, as well as the D706:P(-1) Arg salt bridge remains largely unchanged. The Y701:P(-5) interaction appears more often in some mutants, most prominently in R743H, but still

only to a low extent. In the V677M variant, this Y701:P(-5) bond does not form, but some transient P(-5):R743 salt bridges emerge. In the R679W mutant, W679 not only deforms the binding site but also exhibits a tendency to form a strong H-bond with the carbonyl O of P(-5) Glu, fixing the peptide in a distorted conformation that deviates from the expected β-strand structure. In the G734SQ variant, the H735:P(-2) H-bond occurs with lower frequency, while the alternative interaction formed by H735 to P(-5) has a higher tendency to form.

The R736Q variant forms the highest net number of specific interactions with GKAP. ***(Fig. 4B)*** No salt bridge can form between P(-5) Glu and Q736, which results in P(-5) forming end-on salt bridges with another arginine of the "triad", R743, while simultaneously establishing an H-bond to Q736, which, we predict, together might compensate for the loss of this salt bridge interaction with the mutated R736. ***(Fig. 6)*** This also explains the increased prevalence of H-bonds between H735 and P(-2), as P(-5) can not establish contacts with this histidine in this bent conformation of the peptide. The most prominent changes in the R743H mutant are the lack of the aforementioned carboxylate binding interaction of position 743, diminished H735 interactions and an increased prevalence in the P(-5):Y701 H-bond. ***(Fig. 4B)***

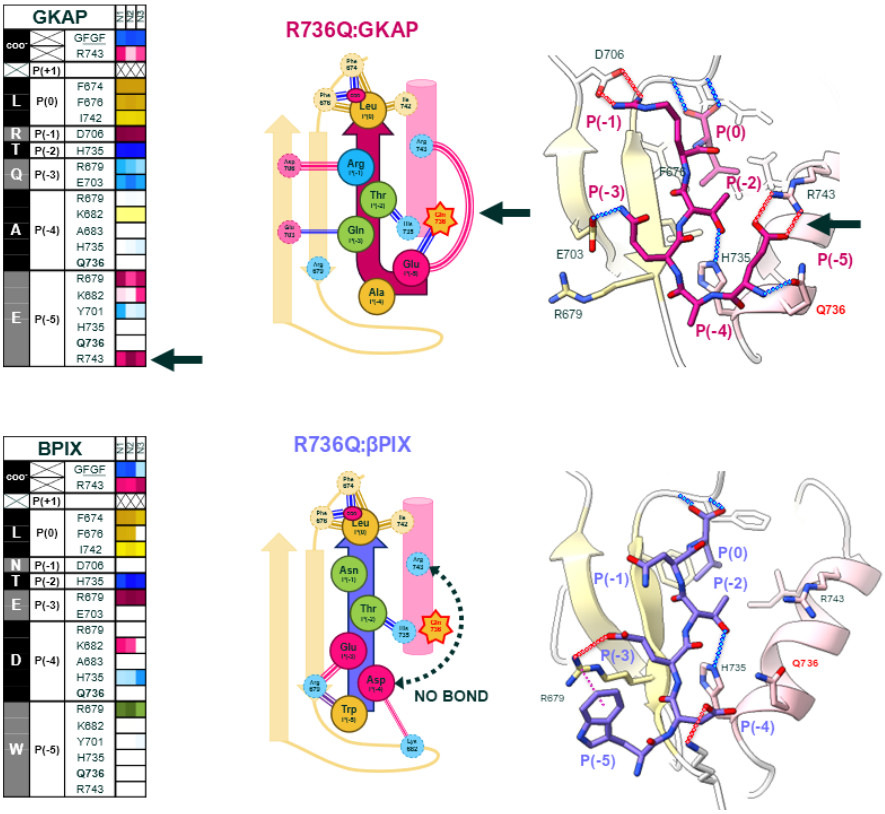

Figure 6. Schematic and 3D models of the R736Q-GKAP and R736Q-βPIX complexes.
In the WT-GKAP interaction, P(-5) forms a salt bridge with R736, which in the mutant is replaced by a transient salt bridge with R743 which results in a strong hydrogen bond with Q736. The analogous interaction to this in the βPIX peptide is the salt bridge between P(-4) and R736 – in the R736Q mutant, this salt bridge is entirely lost and P(-4) does not form alternative bonds. Full a full series of schematic diagrams and figure legends, refer to the Supplementary Material.

Previously unseen cation-π stack in the βPIX interaction varies highly per mutant

The peptide of βPIX exhibits a very stable β-strand conformation in complex with Shank1-PDZ WT but a reduced number of sidechain interactions compared to GKAP. The P(0) Leu remains inserted into the hydrophobic pocket. The H735:P(-2) sidechain H-bond is also more stable, appearing in ~90% of the snapshots, as are the salt bridges formed by Asp P(-4) and Glu P(-3) with R736 and R679, respectively, in accordance with the experimental structure 3QJN and 3L4F. The only major deviation from these X-ray structures is the behavior of P(-5) Trp, which, instead of being inserted into the β2-β3 loop, stacks onto R679 in a cation–π interaction.

In the V677M mutant complex, positions P(0)-P(-2) remain unaffected as expected. The P(-3):R679 salt bridge is slightly weakened, as R679 has a higher tendency to form an intramolecular interaction with E703 (characteristic of the apo structure).

The R679W mutation largely deforms the extended conformation of the bound peptide and the complex is characterized by prominent widespread loss of interactions and partial dissociation. As mentioned earlier, the conserved carboxylate binding H-bond network disappears in favour of the alternative salt bridge to R743.

The simulations of the G734S variant suggest a disorganization of the binding network, with several alternative conformations emerging, such as salt bridges and H-bonds of P(-4) to R679, K682 and H735, and alternative cation–π stacking by P(-5) to R736. The repeated runs are highly inconsistent, suggesting destabilization.

In the R736Q mutant, the salt bridge between P(-4) Asp and R736 can be considered similar to the one formed by P(-5) Glu in GKAP. However, while Glu P(-5) of GKAP can compensate for the lack of the R679 salt bridge in this mutant, by interacting with R743, P(-4) Asp of βPIX, being shorter, can not participate in an analogous salt bridge. ***(Fig. 4B, Fig. 6)***

In the R743H variant, the alternative R736 cation-π stack is also regularly formed during the simulations, resulting in a periodically flipping tryptophane at P(-5).

A delicately balanced sidechain competition in the mTOR peptide is disrupted in the mutant complexes

Although there is no available experimental structure for the mTOR:Shank1 PDZ complex, the PDB entry 8S1R, featuring a similar internal peptide motif (Ac-$_{[P(-5)]}$EESTSFQGP$_{[P(+3)]}$-$CONH_2$), can be used as a proxy reference. Residue P(0) Phe of the mTOR peptide remains inserted into the hydrophobic pocket, and P(-1) Arg forms a salt bridge similarly to GKAP, which is generally stable, however a competing intrapeptide cation-π interaction between P(-1):P(+1) emerges which is less prominent in the WT but varies across mutants. While the frequency of the H735 H-bond with P(-2) Thr is much lower than for GKAP, P(-3) Ser interacts with E703 more frequently than GKAP's P(-3) Gln. Residues P(-5) and P(-4), both glutamates, form competitive interactions with R736 and R679, taking multiple turns over the course of the simulation. In the 8S1R X-ray structure, the sidechains are paired as P(-4)-R736 and P(-5)-R679. Remarkably, H735 prefers forming H-bonds to either of these glutamates rather than to P(-2) Thr. K682 can also form salt bridges with either of the two glutamates, but not with both simultaneously. Overall, P(-5) and P(-4) dynamically interact with R679, K682, H735 and R736 to a nearly equal extent.

Similarly to that observed for βPIX, the effect of the V677M replacement is towards P(-3) instead of P(-1). The P(-1) salt bridge forms generally less frequently, and a salt bridge between P(-5):R743 emerges.

In the R679W mutant, many interactions are missing. The W679 sidechain is unable to form any salt bridges, and the alternative salt bridges to R736 and K682 fail to compensate for it, as they don't appear in significantly higher frequency than in the other mutants. Interestingly, R743 does not participate in any salt bridges to the peptide, which would be another opportunity to compensate for the lost interactions.

The G734S and R743H mutants are characterized by highly variable interaction patterns throughout the simulations, especially in the P(-1) salt bridge. In R743H, interactions with H743 do not occur, and in one case, the increase in the P(-5):Y701 H-bond emerged, similarly to the GKAP simulation.

In the R736Q mutant, significant loss of the P(-1) Arg salt bridge was observed, in favour of the intrapeptide cation-π stack, to an extent not observed in any of the other variants. The loss of the ionic interaction between P(-5) Glu and the mutated R736 can only be partially compensated by R743 because of the competition with R679, with which P(-4) Glu can also interact. H735 remains H-bonded to P(-2) Thr, similarly to the R736Q:GKAP interaction. ***(Fig. 4B)***

H735 exhibits unique alternative H-bond in ARAP3

For this complex, comparisons can be made with the experimental structure 7A9B. While most interactions described for this X-ray structure are observed in our simulations, the H-bond between Ser P(+1) and D706 does not seem to be stably formed neither in the WT domain nor most of the mutants. In the wild type complex, P(-3) Ser forms a stable H-bond with E703. Besides the Class I characteristic sidechain-sidechain H-bond to P(-2), the side chain of H735 also forms an alternative interaction with P(-4) Thr, creating two conformational clusters. ***(Fig. S3)*** The P(-5) Asp forms a salt bridge with R679, and, with lower frequency, also with K682, R736 and in some cases, even R743.

The V677M mutant exhibits a similar pattern with the notable exceptions of an increase in P(+1):D706 H-bonds. A disruption in the ratio of the two alternative H735 interactions (in WT, the conserved interaction is consistently, strongly preferred) can also be observed in V677M, as well as the rest of the mutants. The R679W mutant shows a tendency to partially dissociate from the partner peptide. G734S exhibits an increase in the P(-5):Y701 H-bond. R736Q, similarly to the case of βPIX, is characterized by the loss of salt bridges at the mutated position, as well as no R743 interaction compensating for it. ***(Fig. 4B)***

Overall, the observed differences between the mutants are mostly subtle, with the exception of the dissociating R679W mutant.

ATG13 binding is dominated by H-bonds and nonpolar interactions

ATG13 is the only analyzed peptide with no similar experimental structure available. The interaction pattern of WT-ATG13 appears to be dominated by H-bonds and hydrophobic interactions throughout the length of the peptide. The C-terminal P(+1) Ser forms a H-bond with D706 in less than 10% of the frames, and P(-1) Ser does not participate in any sidechain interactions. The only other prominent sidechain H-bonds in the whole peptide are formed between P(-3) Thr and R679 as well as E703, with a frequency of about 20-50% for both. Contrary to our expectations, the hydrophobic residues in the 680-690 segment of the β2-β3 loop do not contribute to the accommodation of P(-4) Cys and P(-5) Val, instead, the loop remains extended and the hydrophobic sidechain segments face the PDZ backbone.

The interaction pattern varies only little for most of the mutant PDZ domains. Similarly to the case of ARAP3, V677M exhibits a slight increase in the P(+1):D706 H-bond, and the mutants differ in their loop dynamics, but no other notable differences can be highlighted. The only exception is the complex with R679W which completely dissociates. ***(Fig. 4B)***

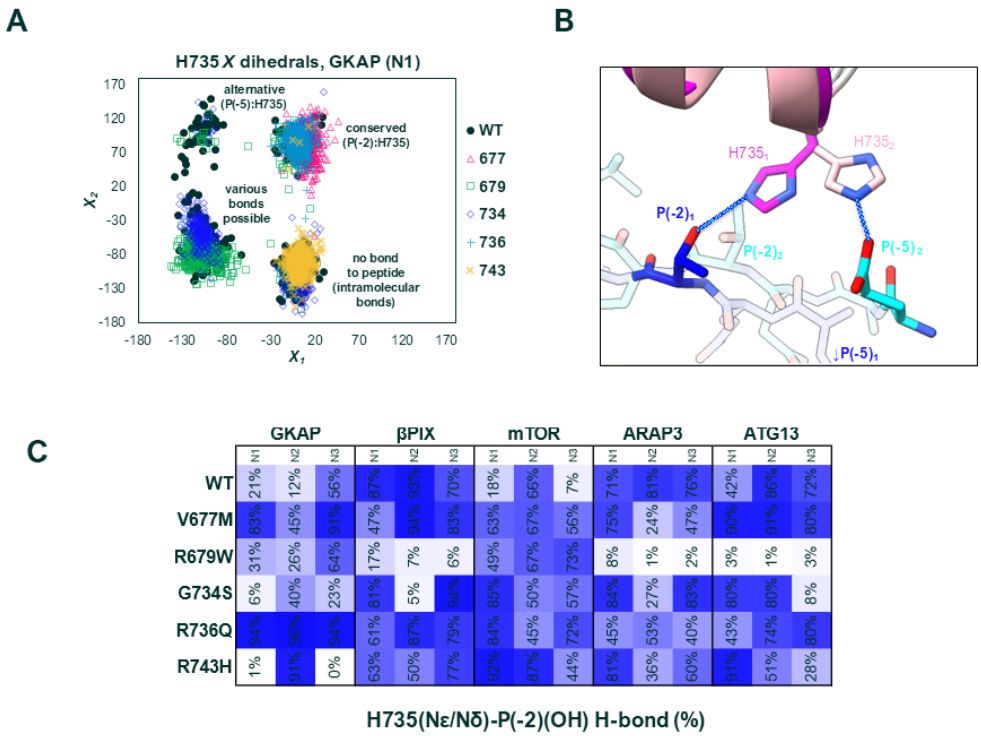

Figure 7. Dynamics of the H735 sidechain. **(A)** X_1-X_2 dihedrals explored by the H735 sidechain during WT-GKAP binding. Note that the X_1-axis was shifted by 180° for better visualization. Each cluster is labelled with the sidechain bond that is probable to occur in said conformation. **(B)** Structures representing two possible extreme conformations of H735 and its H-bonds in the WT-GKAP complex. Darker colors denote the conserved conformation, which is labelled „1". Possible H-bonds in each conformation are represented with blue, dashed lines. **(C)** Summary table showing the presence of the characteristic H735 H-bond throughout MD simulations as percentage, with proportional color intensity. Note that this data is nearly identical to what is seen in Fig. 4B, however the latter also includes bonds where the backbone of the peptide is involved, while this table only shows sidechain-sidechain bonds.

Discussion

Overview of the mutations

All of the most frequent Shank1 PDZ mutations listed in the COSMIC database affect binding site residues. Considering that besides the binding site, the β2-β3 loop, unique to Shank PDZ domains, is also highly conserved in the family, this distribution of the mutations is not necessarily trivial.

Moreover, all the affected residues are located on the surface of the domain, with their sidechains pointing towards the solvent. Therefore, the large changes observed in thermal stability were rather surprising as changing these residues is not expected to disrupt internal residue networks. Perhaps a simple but partial explanation can be provided for the R679W mutant where the R679-E703 salt bridge is disrupted. However, the small destabilizing effect of a Gly to Ser change in G734S and the increased stability in R736Q can not be easily explained on the basis of individual residue properties or clearly identifiable interactions. It should be noted that several X-ray structures of Shank1 PDZ indicate the presence of PDZ dimers (Ali et al., 2021; Im et al., 2003; J. H. Lee et al., 2011; Zeng et al., 2016) that might, in theory, increase the number of residue-residue interactions that should be considered when interpreting mutation effects. Our previous NMR study (Sánta et al., 2022) indicated that the Shank1 PDZ is monomeric in solution, and we have not observed any deviations from the expected molecular mass during protein purification. Thus, although the possibility of dimerization, especially upon ligand binding, cannot be completely dismissed for all variants, we chose to interpret the effects on the monomeric structure as the simplest plausible model.

MD simulations indicated only subtle differences between the global structure of the mutant PDZ domains in the complexes, with the largest changes observed for the β2-β3 loop. As could be expected, this region showed high flexibility and explored a wide range of conformations, with its helical propensity ranging from 1-48% (G, H, I and T states as assigned by DSSP). ***(Fig. 5A)*** The whole loop, spanning positions 680 to 700, is about one fifth of the length of the canonical domain, while it provides a relatively even larger solvent-accessible surface area, about one fourth of the total of the full PDZ. The mutations that caused the highest instability were V677M, R679W and G734S - the first two being the closest to the loop in the sequence, while 734 being in close spatial proximity in the structure.

Dynamics of alternating interactions might be a key contributor to ligand selectivity and binding affinity

Molecular dynamics simulations can capture important aspects of the dynamic behavior of biomolecules, but can not necessarily be expected to accurately reflect all aspects of the actual conformational fluctuations and the delicate balance between all interactions, especially for the diverse systems investigated in this work. Thus, we interpret our analysis as a semiquantitative description that can shed light on several important dynamic aspects and possible interactions, but the actual dynamic balance between the observed conformational states might not be precisely captured.

The most remarkable general observation in our molecular dynamics calculations was the presence of a number of competing interactions. Most of these are alternative salt bridges, like the one formed by the C-terminal carboxylate and R743, which, in turn, also can pair with Asp/Glu residues at position P(-5). This is somewhat surprising given the expected distance between residues P(0) and P(-5) in the extended conformation of the peptide, but during our simulations, the overall flexibility of the complex allowed the formation of both interactions by R743.

Another important dynamic interaction is formed by the conserved H735 imidazole side chain with the residues in the peptides in positions P(-2), P(-4), and P(-5). ***(Fig. 4B, Fig. 7)*** This interaction varies largely for the different peptides and PDZ mutants, ranging from a highly dynamic scenario in the case of GKAP and WT PDZ, where intramolecular H-bond formation is also observed, to the stable H-bond with residue P(-2) in the complexes with ATG13 and βPIX. ***(Fig. 6)*** The difference in the behavior of H735 with different partner peptides suggests a role of H735 in partner selectivity. This is rather unexpected as H735-P(-2) was believed to be a static interaction with the only role of stabilizing the peptide. It should be noted that our molecular dynamics simulations can not account for the changes of the protonation state of the imidazole ring, which might also contribute to the variability of the interactions.

Functional equivalence of side chains in different peptides

We have also observed interactions from the peptide side that can more or less replace each other, suggesting the presence of some degree of functional equivalence between sequential positions in the partner peptides. For example, amino acid residues in peptide positions P(-1) and P(+1), typically positively charged ones, are often interacting with the PDZ residue D706. On the other hand, E703 tends to form an H-bond with P(-3), most commonly a serine in both internal and C-terminal ligands. P(+1), P(-1) and P(-3) tend to always remain pointing towards and interacting with the β-strand side of the binding pocket, a common orientation seen in similar PDZ domains. (H.-J. Lee & Zheng, 2010)

Positions P(-4) and P(-5) show considerable variability, but with a preference towards glutamate or aspartate. Side chains in both positions can form salt bridges with the PDZ residues R679 and R736. Hydrophobic sidechains are also common in these two positions, and if present, they are accommodated by the β2-β3 loop. Our simulations suggest that the interactions formed by P(-4) and P(-5) can drastically influence the backbone conformation of the peptide, with a R736:P(-5) or R743:P(-5) interaction consistent with the emergence of a kinked structure, while hydrophobic interactions with the P(-4)-P(-5) positions result in altered β2-β3 loop dynamics in the PDZ.

For some of the interactions, the sum of intermolecular sidechain bonds correlates well with binding affinity, highlighting the example of the R736Q mutant: compensatory interactions are formed which restore the stability of the complex in the GKAP interaction, while this phenomenon is not observed during, for example, βPIX binding, resulting in the loss of a significant salt bridge. ***(Fig. 6)*** However, not all of the simulations can be interpreted in such a straightforward manner. While in general, the β-sheet propensity of the peptide should be a good approximator of complex stability, those exhibiting a kinked peptide conformation were an exception from this rule and therefore a stable complex could exist even if the extended β-sheet structure does not fully form. Moreover, considering the relatively weak nature of the interactions (micromolar range, even using the measurement techniques that produced the lowest K_d values), it is a possibility that energetic contribution of overall PDZ stability versus the peptide binding network are on par, creating the complex response to the mutations observed in the experimentally determined binding affinities.

Understanding the relationship between binding affinities and mutation induced structural perturbations is further complicated by the apparent dynamic nature of the peptide binding. Several transient, competing interactions were suggested by the MD simulations, including that of the C-terminal carboxylate and H735, previously considered to be stable interactions due to their conserved nature. This, in addition to the dynamics of P(-5) in relation to R679-R736-R743 that was also proposed by previous studies (Hegedüs et al., 2021) and the remarkable mobility of the β2-β3 loop paints a picture of a highly flexible complex.

Possible consequences of the Shank PDZ mutations in associated diseases

All of the partner peptides analyzed in this study have potential or proven connections to disease pathways. Most notably, Shank proteins all have an essential role in regulating postnatal brain development via the Akt/mTOR pathway, however, little is known about the contribution of its individual domains. (Burbach, 2016) The GKAP-Shank interaction via the PDZ domain is crucial as it tethers various other PSD proteins to the NMDA receptors, consequently, GKAP is often described as the main interaction partner of the Shank-PDZ. However, the contribution of this complex to the aforementioned growth factor pathway is elusive. (Naisbitt et al., 1999) Involvement of Shank2 in oncogenesis can be explained, at least in part, by the requirement of the interaction between the Shank2-PDZ and βPIX to regulate Hippo signaling. (Xu et al., 2021) For the remaining two peptides investigated in this study, we found no direct evidence in the literature on how they influence Shank1 function, however, ATG13 is also a member of the TOR pathway and is involved in autophagy, while ARAP3, similarly to βPIX, is involved in GTPase mediated

signaling and regulates cytoskeletal remodeling. (Jung, Ro, Cao, Otto, & Kim, 2010; Myers & Casanova, 2008)

Loss of Shank function can be one of the mechanisms behind ASD, as observed in Phelan-McDermid syndrome and experiments with KO and KI mice. (Hagmeyer, Sauer, & Grabrucker, 2018; Qin et al., 2022; Sungur, Vörckel, Schwarting, & Wöhr, 2014) Conversely, overexpression of Shank proteins is oncogenic. (Chen et al., 2022; Wang et al., 2020; Xu et al., 2021) Interestingly, all of the cancer associated mutations analyzed in our study turned out to be destabilizing, loss-of-function mutations, while the one found in also ASD was the mutant with increased stability. However, as the above example with βPIX and the Shank2 PDZ shows, loss or gain of function in a single domain does not necessarily translate to models of under- and overexpression respectively. Instead, in an interaction network as abundant and complex as the one Shank1 is centered at, the perturbing effects of a mutation might require an explanation within a larger context. Our results show that each disease-associated mutation has its own unique pattern in affecting the five interactions, to which overall domain stability was only a partial contributor. This suggests a highly complex perturbing effect on the interaction network of the domain, with binding preferences shifting from one partner to another in some cases. Systems biology simulations had recently demonstrated that small changes in the initial conditions, such as a single K_d value, can result in a large nontrivial perturbation on the PSD interaction network. (Miski et al., 2023) Experimental data like ours can be used as input to refine such modeling approaches to address similar systems more realistically.

Our results highlight the intricate interplay of residue-residue interactions in partner binding and show that the effects of mutations can be highly partner-specific in the case of a promiscuous partner binding domain. We believe that the complex analysis of multiple affected interactions like our study can contribute to a more comprehensive description of the rewiring of protein:protein interaction networks upon specific mutations, leading to a deeper understanding of the interplay between molecular-level changes and phenotypes.

Materials and Methods

Selection of mutations and interaction partners for the study

The only ASD associated missense mutation on the PDZ domain of Shank1, the R736Q variant, had been described by Sato *et al.* (Leblond et al., 2014; Sato et al., 2012) Other cancer associated somatic variants were collected from the COSMIC database. (Sondka et al., 2024) In this case, the four most frequent variants (at the time of data collection) of the region were chosen for the study. Where multiple variants were documented at the same position, the most frequent was picked. The C-

terminal peptide of GKAP was chosen as the first model system as it is the most studied, and the additional peptides were chosen with the following considerations: diversity in binding motifs; diversity in associated GO terms; preference for ligands with existing experimental structures in complex with the Shank1-PDZ; preference for ligands with K_d values known from literature. Peptides for experiments were designed based on peptide constructs with known K_d values found in papers associated with PDB structures. (Ali et al., 2021; J. H. Lee et al., 2011; Zeng et al., 2016)

Expression of constructs

The wild type Shank1 PDZ domain and its missense variants as well as the 186 amino acid long C-terminal segment of GKAP (GKAP GH1) were expressed in *E. coli* strain. The Shank1 PDZ construct spans from G654 to K768 on the human Shank1 reference sequence (NP_057232.2, Q9Y566-1). A rat Shank-1 ORF plasmid (kindly provided by Enora Moutin from the University of Geneva) was used to amplify the insert for cloning. Note that in this region, Rat and Human ORFs code for the same protein sequences. The insert was ligated into NdeI and BamHI sites of a modified pET-15b vector (Novagen) that contains a tobacco etch virus (TEV) protease cleavage site instead of the thrombin sequence. The expressed construct is equipped with an N-terminal 6xHis tag. Missense mutations were introduced into the Shank1 PDZ plasmid by site directed mutagenesis using PCR primer pairs bearing the desired mutation for the amplification of the whole plasmid. The construct coding the C-terminal segment of GKAP (GKAP GH1) corresponds to the rat GKAP1a D481-L666 region (Uniprot P97836-5) and its insert was picked up from a rat GKAP1a ORF template kindly provided by Enora Moutin. This 186 amino acid long segment differs from the human GKAP sequence of 792-977 only at K501 (Uniprot P97836-5), the human protein (Q9D415-1) has a glutamine amino acid at this position. This insert was ligated into the same modified pET-15b plasmid as used for Shank1 PDZ. The GKAP construct labelled CT43 is 100% identical to the human sequence covering residues 935-977 and was created using the same methods. Constructs coding 12 amino acid long peptides incorporating the binding motifs of GKAP, βPIX, ARAP3, mTOR and ATG13 were designed based on the human protein sequences (Uniprot entries Q9D415-1, Q14155-1, Q8WWN8-1, P42345 and O75143-1 respectively), using peptides listed by Ali et al. as a template. (Ali et al., 2021). In vitro mutagenesis was used to introduce the sequences into a pGex-4T1 vector, resulting in a GST-tagged construct containing a thrombin site ***(Table S1)***.

Protein purification

Protein expression from all constructs were induced in BL21 (DE3) cells (Novagen) with 1 mM IPTG at 4 MFU cell density and the recombinant proteins were expressed

at 20 °C for 16 h in LB medium. Cell pellets were lysed by ultrasonic homogenization in 10% cell suspension using a lysis buffer (50 mM NaPi, 300 mM NaCl, pH 7.4). After homogenization, cell supernatants were purified by IMAC using 5 ml Nuvia™ Ni-affinity column (Bio-Rad), followed by His-tag removal from Shank1-PDZ proteins with TEV protease. Proteins were further purified by ion exchange chromatography, using 5 ml High Q column for Shank1-PDZ constructs (recombinant Shank protein was collected in the flow through fraction) and High S columns for the GKAP GH1 construct (recombinant GH1 was eluted by NaPi buffer with 1 M NaCl). Protein samples were concentrated by ultrafiltration using Amicon® Ultra Centrifugal Filter with 3 kDa molecular weight cut off value, and the buffer of recombinant proteins was changed to low salt NaPi Buffer (50 mM NaPi; 20 mM NaCl, 0.02% NaN3; pH 7.4). The concentration of the proteins was measured by their absorbance at 280 nm using a NanoDrop2000 photometer, while their purity and exact molecular weight was analyzed by SDS-PAGE and LC–MS. Before pull-down and BLI assays, Shank1 PDZ constructs were purified additionally by reverse IMAC (the protease-treated sample is loaded onto an IMAC column - the cleaved protein remains in the flowthrough fraction) in order to get rid of trace amounts of His-tagged protein and peptide impurities. In the course of this step 20 mM of imidazole and 0.02% Tween 20 as well as 30 µl of equilibrated Nuvia™ IMAC resin was added to every mg of IEC purified PDZ samples followed by a 2 min RT incubation with gentle but thorough mixing. The beads were sedimented by centrifugation, and the flow-through was retained. The production of the GST-tagged 12 amino acid peptide constructs was identical up to the purification steps. Cell lysates were then loaded onto a Bio-Rad Poly-Prep® Chromatography Column filled with Cytiva Glutathione Sepharose™ 4B beads. The aforementioned low salt NaPi Buffer was used for the binding step, and the same buffer with additional 20 mM glutathione was used to elute the proteins. No additional steps were used for these constructs because sample purity was sufficient and the glutathione content in the buffer was negligible at the dilutions used for later experiments.

Pull-down experiments

For pull-down assays, the 6xHis-tagged GKAP-GH1 construct was used as the bait and the Shank1-PDZ wild type or its mutants lacking the His-tag

was the prey molecule. The proteins were purified for the assay as stated above. All steps of the protocol were performed in PD buffer (50 mM NaPi; 20 mM NaCl; 0.1% Tween 20; 0.1% BSA; 20 mM Imidazole; pH 7.4). For each reaction, a pellet of 20 µl 50% suspension of Nuvia IMAC beads equilibrated in PD buffer was mixed with 70 µM GH1 protein diluted in 40 µl of PD buffer followed by a 2 min. RT incubation with mild shaking. In case of GH1- WT+ control sample 40 µl of PD buffer was added without GH1 protein. After the incubation, beads were washed 3 times with 150 µl of PD buffer and 75 µM Shank1-PDZ diluted in 30 µl PD buffer was mixed with the pellet of beads. In case of GH1+ Shank1-PDZ – control sample PD buffer was added without Shank1-PDZ protein, while wild type Shank1-PDZ was added to the GH1- WT+ control sample. Addition of the prey was followed by a 2 min. RT incubation and three wash steps, then 20 µl of elution buffer (0,5 M Imidazole in PD buffer) was added to the pellet of beads. After a 2 min. RT incubation with mild shaking, 15 µl of 3x Laemmli buffer was added to the samples followed by an additional 2 min. shaking incubation. SDS-PAGE images were analyzed with ImageJ. (Schneider, Rasband, & Eliceiri, 2012)

Biolayer Interferometry

Prior to experiments, all Ni-NTA biosensors (Fortebio, USA) were hydrated in kinetic buffer (50 mM NaPi pH 7.4, 20 mM NaCl, 20 mM imidazole, 0.1% BSA, 0.02% Tween 20, 0.02% N3Na) at 25°C for 10 min. The ligand, the 6xHis-tagged GH1 or CT43 protein was immobilized on the surface of the biosensor at a 5 µg/ml concentration in kinetic buffer for 120 sec. The initial baselines were then recorded in kinetic buffer for 30 s using a BLItz system (ForteBio, USA). The association and dissociation sensorgrams of WT and mutant PDZ domains at concentrations ranging from 0.5 µM to 4 µM were recorded for 30 sec each in kinetic buffer, too. The equilibrium dissociation constant (K_d) was determined from the BLI data at various concentrations of the PDZ domains using the global fitting method provided in the BLItz data analysis software. The BLI experiments with the anti-GST biosensors were conducted nearly identically, with the following exceptions. Imidazole was omitted from the kinetic buffer. The GST-tagged proteins were diluted to 20 µg/ml, and the PDZ domains were measured at concentrations ranging from 1.25 µM up to 60 µM. Association and dissociation steps were extended to 60 s.

Fluorescence polarization spectroscopy

Interaction of FITC-labeled CT12 GKAP peptide (FITC-IEIYIPEAQTRL, BioBasic) with the wild type and mutant Shank1-PDZ samples were measured in kinetic buffer (50 mM NaPi pH 7.4, 20 mM NaCl, 20 mM imidazole, 0.1% BSA, 0.02% Tween 20, 0.02% N_3Na) at 25°C. Series of 1.7 fold dilutions of the PDZ domains were prepared (70 µl of sample into 100 µl of kinetic buffer) with 50-150 µM starting concentrations. The

concentration of the FITC-C12 peptide was 10 nM constant in all samples except the reference blank sample, where no peptide was added. Fluorescence polarization of the samples was measured in a black, flat 96 well plate (Greiner bio-one) in duplicates (100 µl / rxn) using a Spark 20M multimode microplate reader (TECAN) in filter mode. No Shank was added in the Reference samples, while in the Reference blank there was neither Shank, nor peptide. G-factor was estimated to be 1.067. The equilibrium dissociation constants (K_d) were calculated from the inflection point of the fitted titration curves.

Thermal shift assay

Shank1-PDZ protein samples were analyzed in 0.2 µg / µl final concentration in low salt NaPi buffer supplemented with Sypro Orange dye in 5x final concentration. Duplicates of 25 µl samples were analyzed in a PikoReal real-time PCR instrument. The temperature was elevated from 30 °C to 80 °C with a 0.2 °C / 30 sec increment followed by 30 sec incubation and data collection protocol. Fluorescent data was collected in the SybrGreen channel. The negative derivative of the RFU was plotted as a function of temperature in order to get melting temperature values as the peak of the melting curves.

ECD spectroscopy

Wild type and mutant Shank1-PDZ proteins were measured by ECD spectroscopy using JASCO J-1500 spectrometer (JASCO Corporation, Tokyo, Japan). All samples were diluted to 7 µM in low salt NaPi buffer. ECD spectra were recorded at 30 °C using 0.1 cm path length J/21 quartz cuvette (Jasco Corporation) and 300 µl sample with the following settings: 195–260 nm spectral range, 50 nm/min scanning speed, 1 nm bandwidth, 0.2 nm step size, 0.5 s response time and 3 scans of accumulation and baseline correction. For melting experiments, temperature scan measurements were carried out with the same settings above. Full ECD spectra were recorded at increasingly higher temperatures starting with 30 °C up to 70 °C in 5 °C increments. Thermal denaturation of the protein samples was demonstrated by the decrease of CD values at 200 nm and the increase at 210 nm, since these changes reflect the increase in the proportion of random coils.

Peptide docking

The WT and mutant PDZ domains in complex with a C-terminal peptide "EAQTRL" of GKAP and apo PDZ domains were modelled in UCSF Chimera 1.18 (Pettersen et al., 2004) using MODELLER (Webb & Sali, 2016) and refined with FoldX (Schymkowitz et al., 2005), using structure 1Q3P from the PDB as a starting point. These structures were then used as templates for docking simulations. Peptides were docked using AutoDock Crankpep (ADCP). (Y. Zhang & Sanner, 2019) First, a structural model for the WT

domain in its apo form was created as described above, then the peptides "EAQTRL", "WDETNL" and "DTSTSFS", corresponding to GKAP, βPIX and ARAP3, respectively, were docked into this model, and then compared to the experimental structures available under the PDB IDs 1Q3P, 3QJM and 7A9B, respectively. For more details on PDB structures and constructs, see ***Table S1***. RMSD scores between corresponding structures were calculated in UCSF ChimeraX 1.8 (Meng et al., 2023), with sidechains compared only up to the Cβ atoms. This is due to the ADCP output producing incomplete ligand sidechains, where each sidechain is represented by only a Cβ-Cγ pair with varying length of the covalent bond to represent volume. These RMSD scores remained below <1 Å for all three complexes, therefore we concluded that the method reproduces the experimentally determined bound conformations sufficiently well. Then, the remaining two peptides were docked into the same model ("EESTRFY" of mTOR and "VCTTSFS" of ATG13) and all docking calculations were repeated for each of the PDZ mutants.

Molecular dynamics simulations and analysis of structural ensembles

Explicit solvent molecular dynamics simulations of WT and all mutants paired with each ligand peptide were performed with GROMACS (Páll et al., 2020) on the Komondor supercomputer. The AMBER99SB-IDLN force field was used, with a box setting of 1.0 n minimum distance. An 1000 ns time interval was simulated (for each complex), from which, 500 snapshots were taken. Each simulation was repeated an additional two times, using identical initial parameters, resulting in 90 snapshot ensembles, which we provide in the Supplementary Material in PDB format. The snapshot ensembles were visually inspected in Chimera 1.8. (Pettersen et al., 2004) Structural alignment of the ensembles and RMSD calculations were done with LSQMAN. (Kleywegt, 1996) Secondary structure composition was calculated with DSSPCont. (Carter, Andersen, & Rost, 2003) HBPlus (McDonald & Thornton, 1994) was used to extract lists of possible H-bonds, defined as 4 Å. To calculate specific atom-atom distances, salt bridges, cation-π interactions and X_1, X_2 torsion angle distributions, in-house Perl and Python scripts by Z. Gáspári and Z. Kálmán were used. Nonpolar interactions between two sidechains were defined as within 4.0 Å between their CB atoms, or in case of arginine sidechains, averaged from distance to its CB, CG atoms. For the C-terminal hydrophobic pocket, this constraint was raised to 6.0 Å, due to the larger sidechains involved, and based on the distances observed on X-ray structures. The C-terminal conserved hydrogen bond with the GFGF motif was described by a single number obtained by averaging all such interactions of the F674, G675 and F676 sidechains, including those involving the PDZ backbone. Additionally, FoldX (Schymkowitz et al., 2005), PDBePISA (Krissinel & Henrick, 2007) and CaPTURE (Gallivan & Dougherty, 1999) were used on some individual snapshots for further

verification of findings. Principal component analysis was conducted using the ProDy package. (S. Zhang et al., 2021)

Evaluation and visualization of data

DNA constructs were designed in SerialCloner 2.6.1. (RRID:SCR_014513). Sequence alignment was performed in BioEdit. (RRID:SCR_007361) (Hall, 1999) PCA modes were inspected in VMD. (Humphrey, Dalke, & Schulten, 1996) Other data were evaluated and visualized using Microsoft Excel. An Excel Solver add-in was used for sigmoid curve fitting of FP and CD measurements. (Kemmer & Keller, 2010) Figures were edited in Microsoft Powerpoint.

Supplementary Material

Besides figures and tables cited in the paper, we also provide the following supplementary files: a SupplementaryFigures.pdf document containing a full series of schematic diagrams representing peptide binding modes ***(Fig. S1)***, the PCA results in Fig. 5 separated by peptide as opposed to mutations in the original figure ***(Fig. S2)***, the full series of figures of *X* dihedral angle distributions ***(Fig. S3)*** and the original image of the SDS-PAGE results of Fig. 3A for transparency ***(Fig. S4)***, due to it requiring some editing to remove the incomplete text that was previously accidentally saved onto the image; SupplementaryTables.xls containing experimental data, the sidechain interaction map in Fig. 4B in a numerical format and additional data derived from MD simulations ***(Table S1-S10)***; SupplementaryPDBs.zip containing all 90 PDB snapshot ensemble files.

Author Contributions

Anna Sánta: Conceptualization, Investigation, Formal analysis, Writing - Original Draft, Writing - Review & Editing, Visualization. **Zsófia E. Kálmán:** Investigation, Formal analysis, Writing - Review & Editing. **Eszter Nagy-Kanta:** Investigation, Resources, Writing - Review & Editing. **Zoltán Gáspári:** Writing - Review & Editing, Supervision, Funding acquisition. **Bálint Péterfia:** Conceptualization, Investigation, Resources, Writing - Original Draft, Writing - Review & Editing, Supervision.

Acknowledgments

The authors acknowledge the support of the National Research, Development and Innovation Office - NKFIH - through grant OTKA K 137947 (to Z.G.), and the Digital Government Development and Project Management Ltd. for awarding us access to the Komondor HPC facility based in Hungary. The authors express gratitude for the contributions of: Enora Moutin for providing cDNA constructs, Viktor Farkas for the assistance with CD measurements, and Zsuzsanna Stránerné Szabó, Anna Oláh, József Hegedüs and Melinda Keresztes for their contribution to the experiments over the years.

Conflict of Interest

The authors declare no conflict of interest.

References

Ali, M., McAuley, M. M., Lüchow, S., Knapp, S., Joerger, A. C., & Ivarsson, Y. (2021). Integrated analysis of Shank1 PDZ interactions with C-terminal and internal binding motifs. *Current Research in Structural Biology*, *3*, 41–50. doi: 10.1016/j.crstbi.2021.01.001

Burbach, J. P. H. (2016). Unraveling a pathway to autism. *Science*, *351*(6278), 1153–1154. doi: 10.1126/science.aaf5097

Carter, P., Andersen, C. A. F., & Rost, B. (2003). DSSPcont: Continuous secondary structure assignments for proteins. *Nucleic Acids Research*, *31*(13), 3293–3295. doi: 10.1093/nar/gkg626

Chang, C.-F., Huang, S.-P., Hsueh, Y.-M., Geng, J.-H., Huang, C.-Y., & Bao, B.-Y. (2022). Genetic Analysis Implicates Dysregulation of SHANK2 in Renal Cell Carcinoma Progression. *International Journal of Environmental Research and Public Health*, *19*(19), 12471. doi: 10.3390/ijerph191912471

Chen, B., Zhao, H., Li, M., She, Q., Liu, W., Zhang, J., … Wu, J. (2022). SHANK1 facilitates non-small cell lung cancer processes through modulating the ubiquitination of Klotho by interacting with MDM2. *Cell Death & Disease*, *13*(4), 403. doi: 10.1038/s41419-022-04860-3

Gallivan, J. P., & Dougherty, D. A. (1999). Cation-π interactions in structural biology. *Proceedings of the National Academy of Sciences*, *96*(17), 9459–9464. doi: 10.1073/pnas.96.17.9459

Hagmeyer, S., Sauer, A. K., & Grabrucker, A. M. (2018). Prospects of Zinc Supplementation in Autism Spectrum Disorders and Shankopathies Such as Phelan McDermid Syndrome. *Frontiers in Synaptic Neuroscience*, *10*, 11. doi: 10.3389/fnsyn.2018.00011

Hall, T. A. (1999). BioEdit: A user-friendly biological sequence alignment editor and analysis program for Windows 95/98/NT. *Nucleic Acids Symposium Series*, *41*(41), 95–98. Oxford. Retrieved from https://www.academia.edu/download/29520866/1999hall1.pdf

Hegedüs, Z., Hóbor, F., Shoemark, D. K., Celis, S., Lian, L.-Y., Trinh, C. H., … Wilson, A. J. (2021). Identification of β-strand mediated protein–protein interaction inhibitors using ligand-directed fragment ligation. *Chemical Science*, *12*(6), 2286–2293. doi: 10.1039/D0SC05694D

Humphrey, W., Dalke, A., & Schulten, K. (1996). VMD: Visual molecular dynamics. *Journal of Molecular Graphics*, *14*(1), 33–38, 27–28. doi: 10.1016/0263-7855(96)00018-5

Im, Y. J., Kang, G. B., Lee, J. H., Park, K. R., Song, H. E., Kim, E., … Eom, S. H. (2010). Structural Basis for Asymmetric Association of the βPIX Coiled Coil and Shank PDZ. *Journal of Molecular Biology*, *397*(2), 457–466. doi: 10.1016/j.jmb.2010.01.048

Im, Y. J., Lee, J. H., Park, S. H., Park, S. J., Rho, S.-H., Kang, G. B., … Eom, S. H. (2003). Crystal Structure of the Shank PDZ-Ligand Complex Reveals a Class I PDZ Interaction and a Novel PDZ-PDZ

Dimerization. *Journal of Biological Chemistry*, *278*(48), 48099–48104. doi: 10.1074/jbc.M306919200

Jung, C. H., Ro, S.-H., Cao, J., Otto, N. M., & Kim, D.-H. (2010). mTOR regulation of autophagy. *FEBS Letters*, *584*(7), 1287–1295. doi: 10.1016/j.febslet.2010.01.017

Kemmer, G., & Keller, S. (2010). Nonlinear least-squares data fitting in Excel spreadsheets. *Nature Protocols*, *5*(2), 267–281. doi: 10.1038/nprot.2009.182

Kleywegt, G. J. (1996). Use of non-crystallographic symmetry in protein structure refinement. *Acta Crystallographica. Section D, Biological Crystallography*, *52*(Pt 4), 842–857. doi: 10.1107/S0907444995016477

Krissinel, E., & Henrick, K. (2007). Inference of macromolecular assemblies from crystalline state. *Journal of Molecular Biology*, *372*(3), 774–797. doi: 10.1016/j.jmb.2007.05.022

Leblond, C. S., Nava, C., Polge, A., Gauthier, J., Huguet, G., Lumbroso, S., … Bourgeron, T. (2014). Meta-analysis of SHANK Mutations in Autism Spectrum Disorders: A Gradient of Severity in Cognitive Impairments. *PLoS Genetics*, *10*(9), e1004580. doi: 10.1371/journal.pgen.1004580

Lee, H.-J., & Zheng, J. J. (2010). PDZ domains and their binding partners: Structure, specificity, and modification. *Cell Communication and Signaling*, *8*(1), 8. doi: 10.1186/1478-811X-8-8

Lee, J. H., Park, H., Park, S. J., Kim, H. J., & Eom, S. H. (2011). The structural flexibility of the shank1 PDZ domain is important for its binding to different ligands. *Biochemical and Biophysical Research Communications*, *407*(1), 207–212. doi: 10.1016/j.bbrc.2011.02.141

Li, Y., Trinh, C. H., Acevedo-Jake, A., Gimenez, D., Warriner, S. L., & Wilson, A. J. (2024). Biophysical and structural analyses of the interaction between the SHANK1 PDZ domain and an internal SLiM. *Biochemical Journal*, *481*(14), 945–955. doi: 10.1042/BCJ20240126

Lilja, J., Zacharchenko, T., Georgiadou, M., Jacquemet, G., Franceschi, N. D., Peuhu, E., … Ivaska, J. (2017). SHANK proteins limit integrin activation by directly interacting with Rap1 and R-Ras. *Nature Cell Biology*, *19*(4), 292–305. doi: 10.1038/ncb3487

Liu, X., Yuan, M., Lau, B. W.-M., & Li, Y. (2022). SHANK family on stem cell fate and development. *Cell Death & Disease*, *13*(10), 880. doi: 10.1038/s41419-022-05325-3

Loi, E., Moi, L., Fadda, A., Satta, G., Zucca, M., Sanna, S., … Zavattari, P. (2019). Methylation alteration of SHANK1 as a predictive, diagnostic and prognostic biomarker for chronic lymphocytic leukemia. *Oncotarget*, *10*(48), 4987–5002. doi: 10.18632/oncotarget.27080

McDonald, I. K., & Thornton, J. M. (1994). Satisfying hydrogen bonding potential in proteins. *Journal of Molecular Biology*, *238*(5), 777–793. doi: 10.1006/jmbi.1994.1334

Meng, E. C., Goddard, T. D., Pettersen, E. F., Couch, G. S., Pearson, Z. J., Morris, J. H., & Ferrin, T. E. (2023). UCSF ChimeraX: Tools for structure building and analysis. *Protein Science*, *32*(11), e4792. doi: 10.1002/pro.4792

Miski, M., Weber, Á., Fekete-Molnár, K., Keömley-Horváth, B. M., Csikász-Nagy, A., & Gáspári, Z. (2023, October 19). *Simulated complexes formed from a set of postsynaptic proteins suggest a localised effect of a hypomorphic Shank mutation* (p. 2023.10.16.562557). p. 2023.10.16.562557. bioRxiv. doi: 10.1101/2023.10.16.562557

Myers, K. R., & Casanova, J. E. (2008). Regulation of actin cytoskeleton dynamics by Arf-family GTPases. *Trends in Cell Biology*, *18*(4), 184–192. doi: 10.1016/j.tcb.2008.02.002

Naisbitt, S., Kim, E., Tu, J. C., Xiao, B., Sala, C., Valtschanoff, J., … Sheng, M. (1999). Shank, a Novel Family of Postsynaptic Density Proteins that Binds to the NMDA Receptor/PSD-95/GKAP Complex and Cortactin. *Neuron*, *23*(3), 569–582. doi: 10.1016/S0896-6273(00)80809-0

Páll, S., Zhmurov, A., Bauer, P., Abraham, M., Lundborg, M., Gray, A., … Lindahl, E. (2020). Heterogeneous parallelization and acceleration of molecular dynamics simulations in GROMACS. *The Journal of Chemical Physics*, *153*(13), 134110. doi: 10.1063/5.0018516

Pettersen, E. F., Goddard, T. D., Huang, C. C., Couch, G. S., Greenblatt, D. M., Meng, E. C., & Ferrin, T. E. (2004). UCSF Chimera—A visualization system for exploratory research and analysis. *Journal*

of Computational Chemistry, *25*(13), 1605–1612. doi: 10.1002/jcc.20084

Ponna, S. K., Ruskamo, S., Myllykoski, M., Keller, C., Boeckers, T. M., & Kursula, P. (2018). Structural basis for PDZ domain interactions in the post□synaptic density scaffolding protein Shank3. *Journal of Neurochemistry*, *145*(6), 449–463. doi: 10.1111/jnc.14322

Qin, Y., Du, Y., Chen, L., Liu, Y., Xu, W., Liu, Y., … Wang, H. (2022). A recurrent SHANK1 mutation implicated in autism spectrum disorder causes autistic-like core behaviors in mice via downregulation of mGluR1-IP3R1-calcium signaling. *Molecular Psychiatry*, *27*(7), 2985–2998. doi: 10.1038/s41380-022-01539-1

Sánta, A., Czajlik, A., Batta, G., Péterfia, B., & Gáspári, Z. (2022). Resonance assignment of the Shank1 PDZ domain. *Biomolecular NMR Assignments*, *16*(1), 121–127. doi: 10.1007/s12104-022-10069-4

Sato, D., Lionel, A. C., Leblond, C. S., Prasad, A., Pinto, D., Walker, S., … Scherer, S. W. (2012). SHANK1 Deletions in Males with Autism Spectrum Disorder. *American Journal of Human Genetics*, *90*(5), 879–887. doi: 10.1016/j.ajhg.2012.03.017

Schneider, C. A., Rasband, W. S., & Eliceiri, K. W. (2012). NIH Image to ImageJ: 25 years of image analysis. *Nature Methods*, *9*(7), 671–675. doi: 10.1038/nmeth.2089

Schymkowitz, J., Borg, J., Stricher, F., Nys, R., Rousseau, F., & Serrano, L. (2005). The FoldX web server: An online force field. *Nucleic Acids*

Research, *33*(Web Server issue), W382-388. doi: 10.1093/nar/gki387

Sheng, M., & Kim, E. (2000). The Shank family of scaffold proteins. *Journal of Cell Science*, *113*(11), 1851–1856. doi: 10.1242/jcs.113.11.1851

Sondka, Z., Dhir, N. B., Carvalho-Silva, D., Jupe, S., Madhumita, null, McLaren, K., … Teague, J. (2024). COSMIC: A curated database of somatic variants and clinical data for cancer. *Nucleic Acids Research*, *52*(D1), D1210–D1217. doi: 10.1093/nar/gkad986

Sungur, A. Ö., Vörckel, K. J., Schwarting, R. K. W., & Wöhr, M. (2014). Repetitive behaviors in the Shank1 knockout mouse model for autism spectrum disorder: Developmental aspects and effects of social context. *Journal of Neuroscience Methods*, *234*, 92–100. doi: 10.1016/j.jneumeth.2014.05.003

Wang, L., Lv, Y., & Liu, G. (2020). The roles of SHANK1 in the development of colon cancer. *Cell Biochemistry and Function*, *38*(5), 669–675. doi: 10.1002/cbf.3529

Webb, B., & Sali, A. (2016). Comparative Protein Structure Modeling Using MODELLER. *Current Protocols in Bioinformatics*, *54*, 5.6.1-5.6.37. doi: 10.1002/cpbi.3

Xu, L., Li, P., Hao, X., Lu, Y., Liu, M., Song, W., … Jiang, H. (2021). SHANK2 is a frequently amplified oncogene with evolutionarily conserved roles in regulating Hippo signaling. *Protein & Cell*, *12*(3), 174–193. doi: 10.1007/s13238-020-00742-6

Zeng, M., Shang, Y., Guo, T., He, Q., Yung, W.-H., Liu, K., & Zhang, M. (2016). A binding site outside the canonical PDZ domain determines the specific interaction between Shank and SAPAP and their function. *Proceedings of the National Academy of Sciences*, *113*(22). doi: 10.1073/pnas.1523265113

Zhang, S., Krieger, J. M., Zhang, Y., Kaya, C., Kaynak, B., Mikulska-Ruminska, K., … Bahar, I. (2021). ProDy 2.0: Increased scale and scope after 10 years of protein dynamics modelling with Python. *Bioinformatics*, *37*(20), 3657–3659. doi: 10.1093/bioinformatics/btab187

Zhang, Y., & Sanner, M. F. (2019). AutoDock CrankPep: Combining folding and docking to predict protein–peptide complexes. *Bioinformatics*, *35*(24), 5121–5127. doi: 10.1093/bioinformatics/btz459

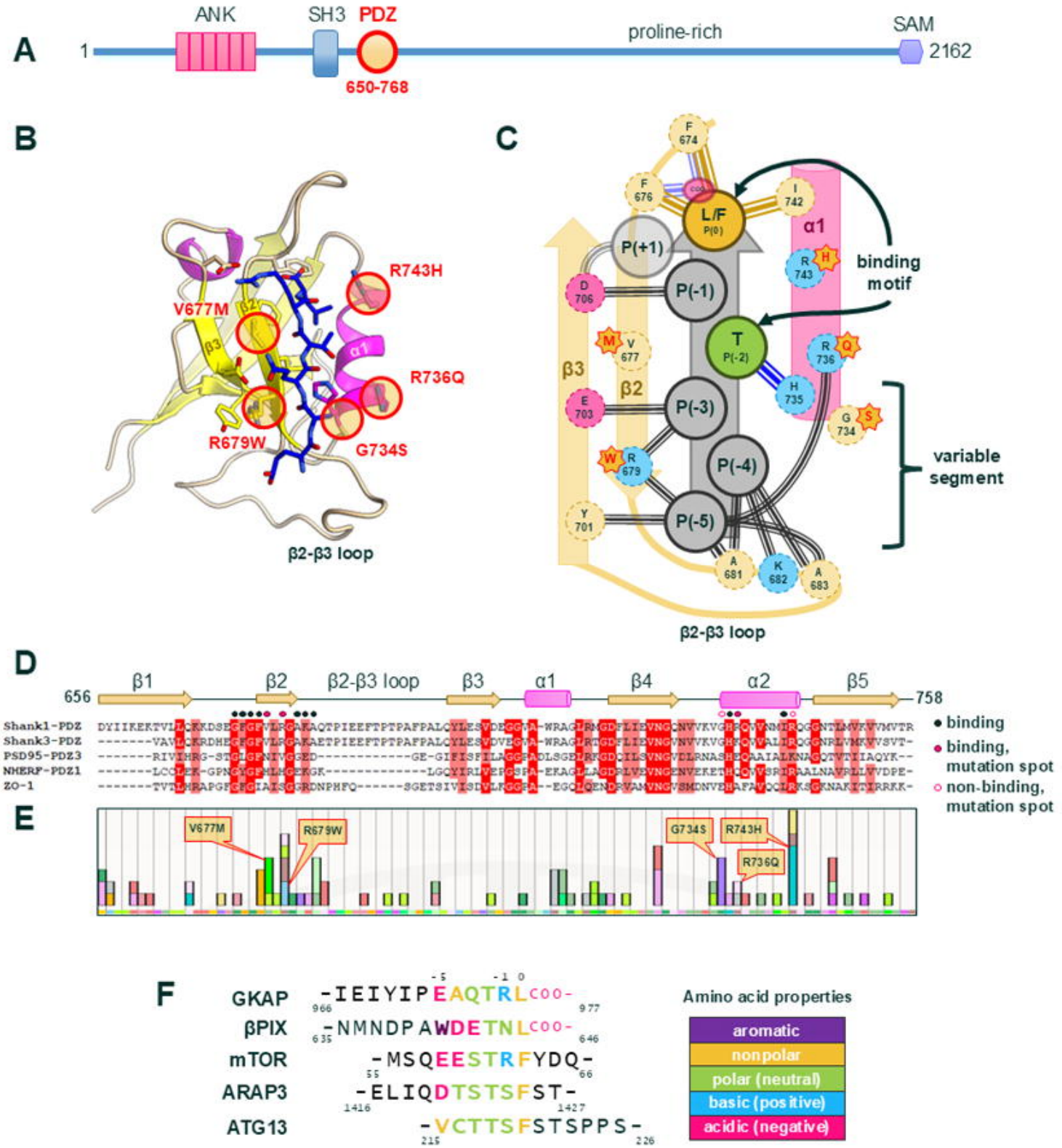
A
1
ANK
SH3
PDZ
650-768
proline-rich
SAM
2162
B
R743H
V677M
R736Q
R679W
G734S
β2-β3 loop
C
L/F
P(0)
P(+1)
P(-1)
T
P(-2)
P(-3)
P(-4)
P(-5)
α1
β3
β2
binding motif
variable segment
β2-β3 loop
D
656
β1
β2
β2-β3 loop
β3
α1
β4
α2
β5
758
Shank1-PDZ
Shank3-PDZ
PSD95-PDZ3
NHERF-PDZ1
ZO-1
binding
binding, mutation spot
non-binding, mutation spot
E
V677M
R679W
G734S
R743H
R736Q
F
GKAP -IEIYIPEAQTRLCOO-
βPIX -NMNDPAWDETNLCOO-
mTOR -MSQEESTRFYDQ-
ARAP3 -ELIQDTSTSFST-
ATG13 -VCTTSFSTSPPS-
Amino acid properties
aromatic
nonpolar
polar (neutral)
basic (positive)
acidic (negative)

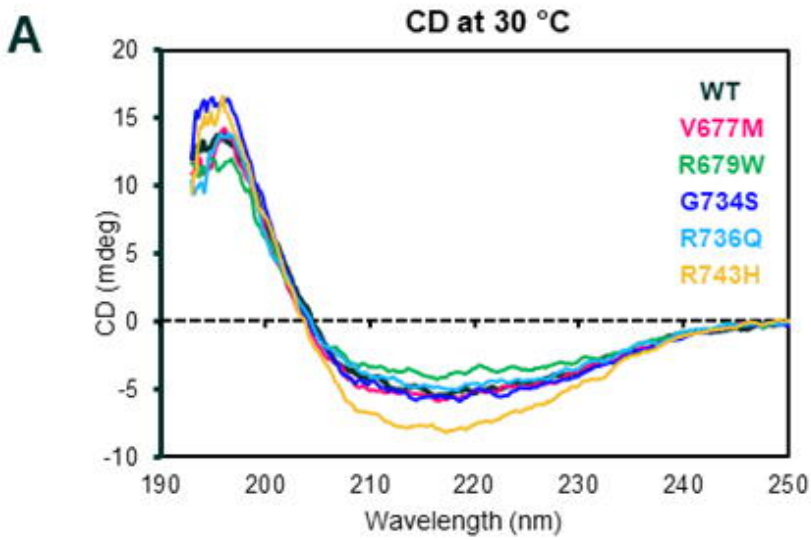
A
CD at 30 °C
WT
V677M
R679W
G734S
R736Q
R743H
CD (mdeg)
Wavelength (nm)
20
15
10
5
0
-5
-10
190
200
210
220
230
240
250

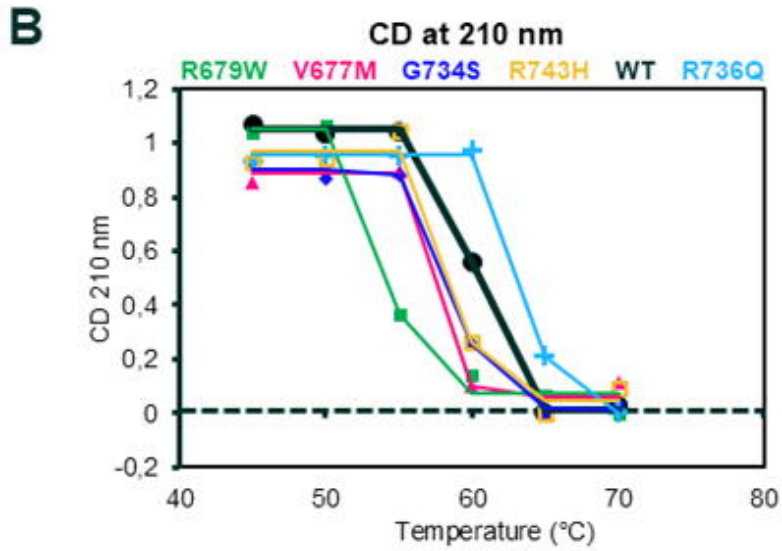
B
CD at 210 nm
R679W
V677M
G734S
R743H
WT
R736Q
CD 210 nm
Temperature (°C)
1,2
1
0,8
0,6
0,4
0,2
0
-0,2
40
50
60
70
80

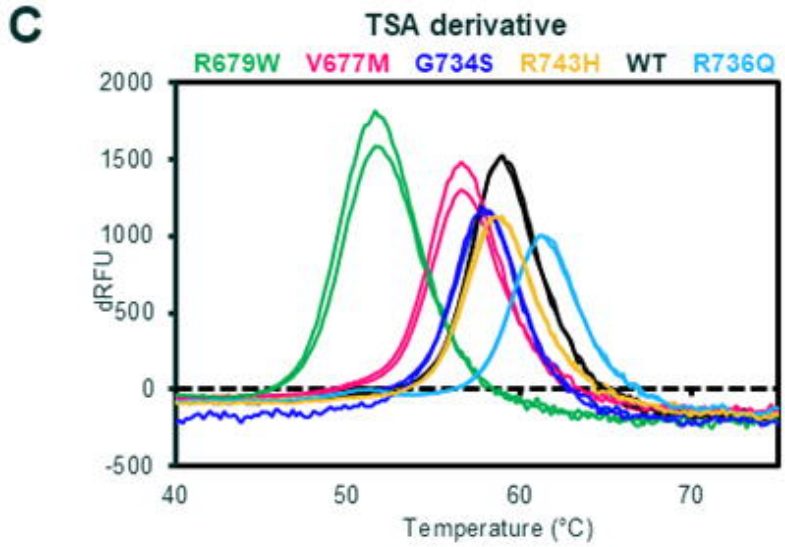
C
TSA derivative
R679W
V677M
G734S
R743H
WT
R736Q
dRFU
Temperature (°C)
2000
1500
1000
500
0
-500
40
50
60
70

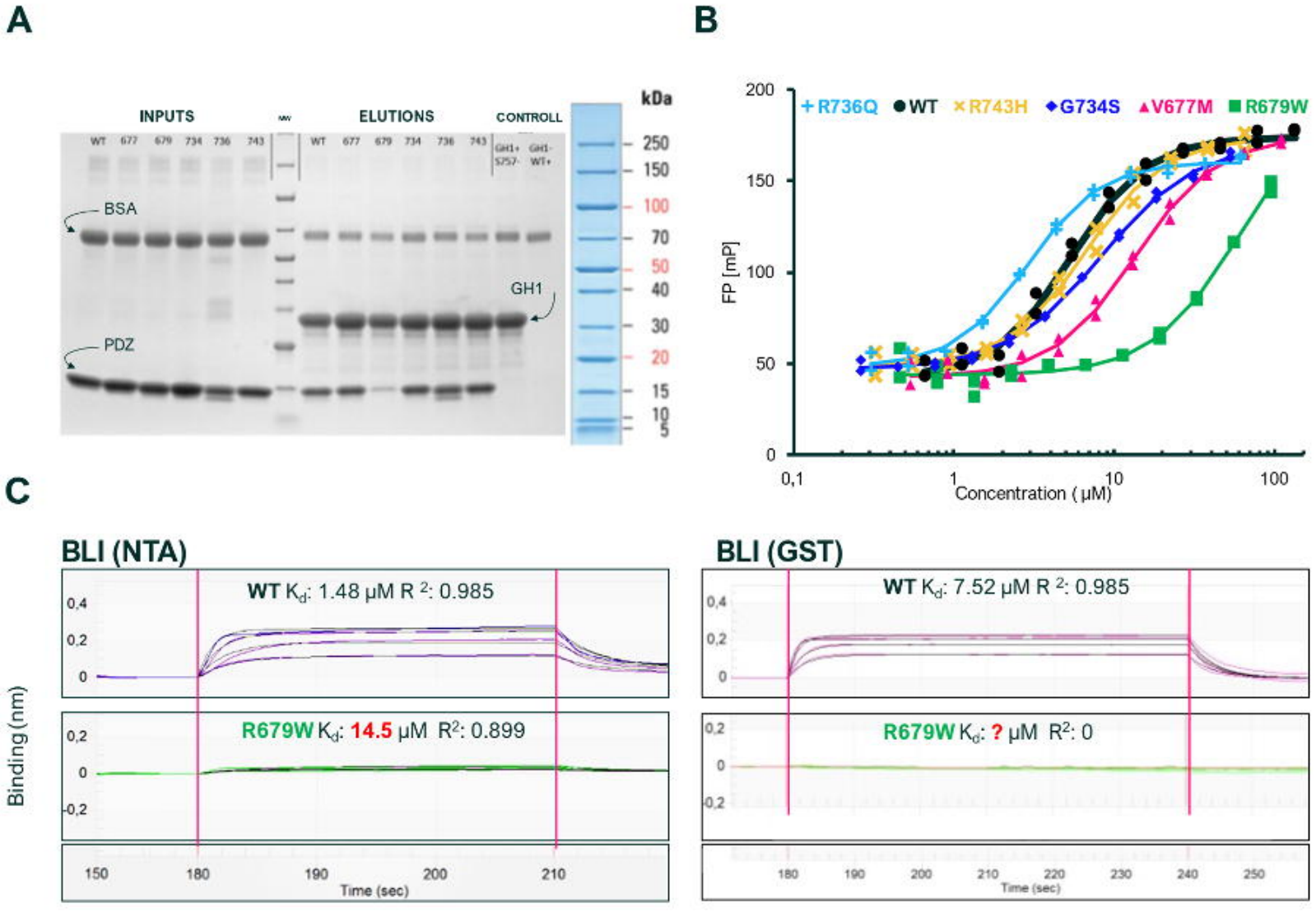
A
INPUTS
ELUTIONS
CONTROLL
WT 677 679 734 736 743
WT 677 679 734 736 743
GH1+ S757-
GH1- WT+
BSA
PDZ
GH1
kDa
250
150
100
70
50
40
30
20
15
10
5
B
R736Q
WT
R743H
G734S
V677M
R679W
FP [mP]
Concentration (µM)
C
BLI (NTA)
WT Kd: 1.48 µM R 2: 0.985
R679W Kd: 14.5 µM R2: 0.899
Binding (nm)
Time (sec)
BLI (GST)
WT Kd: 7.52 µM R 2: 0.985
R679W Kd: ? µM R2: 0
Time (sec)

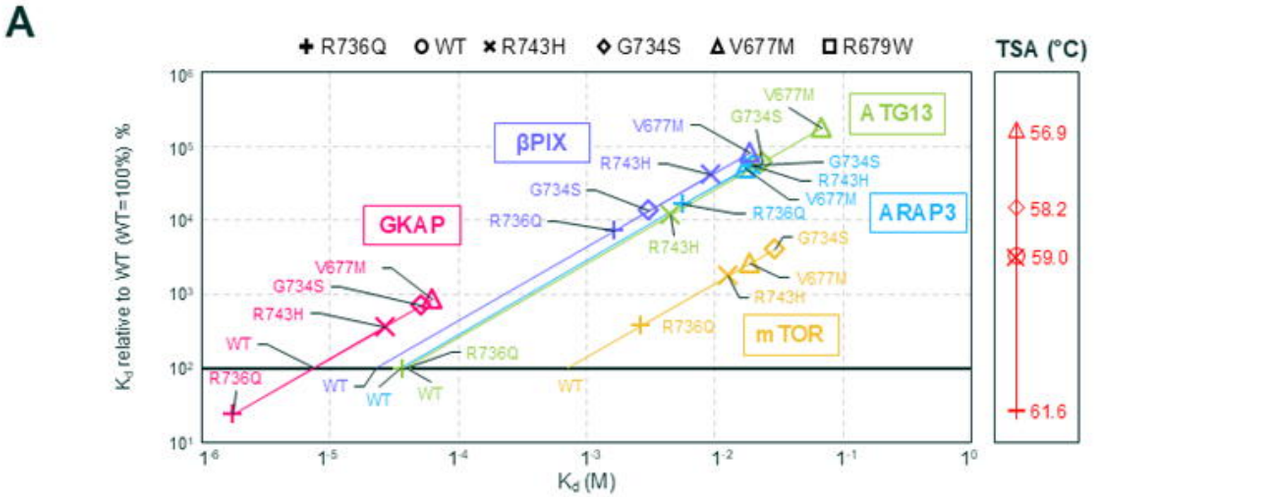

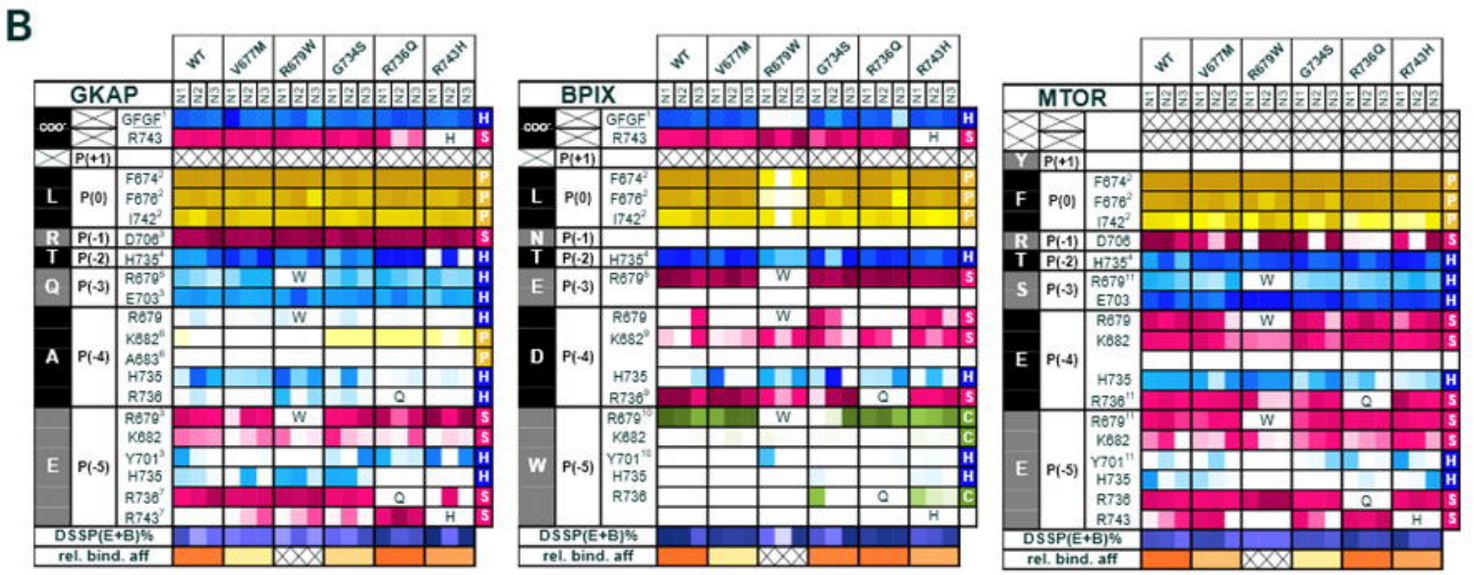

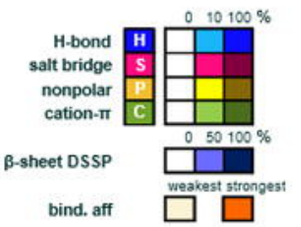

[1]Conserved carboxilate binding motif. (Im et al., 2003)
[2]Hydrophobic cavity accomodating C-terminal sidechain. (Ali et al., 2021; Im et al., 2010, 2010; J. H. Lee et al., 2011; Ponna et al., 2018)
[3]Described in GKAP-bound structures. (J. H. Lee et al., 2011; Ponna et al., 2018)
[4]The H-bond between the imidazole ring of H735 and the OG atom of Thr P(-2) is a signature conserved interaction of Shank1's class of PDZ domains. (Im et al., 2003) Here, H-bonds to the backbone O of Thr P(-2) are also included for consistency – for a table on the conserved H-bond only, see Figure 7.
[5]Described as H-bond in 1Q3P, salt bridge in 5OVC (Im et al., 2003; Ponna et al., 2018)
[6]Described in 5OVC (Ponna et al., 2018)
[7]Suggested by analogous interaction theorized by Hegedüs et al. (Hegedüs et al., 2021)
[8]Described in 3QJN and 3L4F (Im et al., 2010; J. H. Lee et al., 2011)
[9]Described as electrostatic in 3L4F (J. H. Lee et al., 2011)
[10]Described as hydrophobic in 3L4F (J. H. Lee et al., 2011)
[11]Analogous interaction in 8S1R (Li et al., 2024)
[12]Similar interaction in ARAP3-bound 7A9B (Ali et al., 2021)

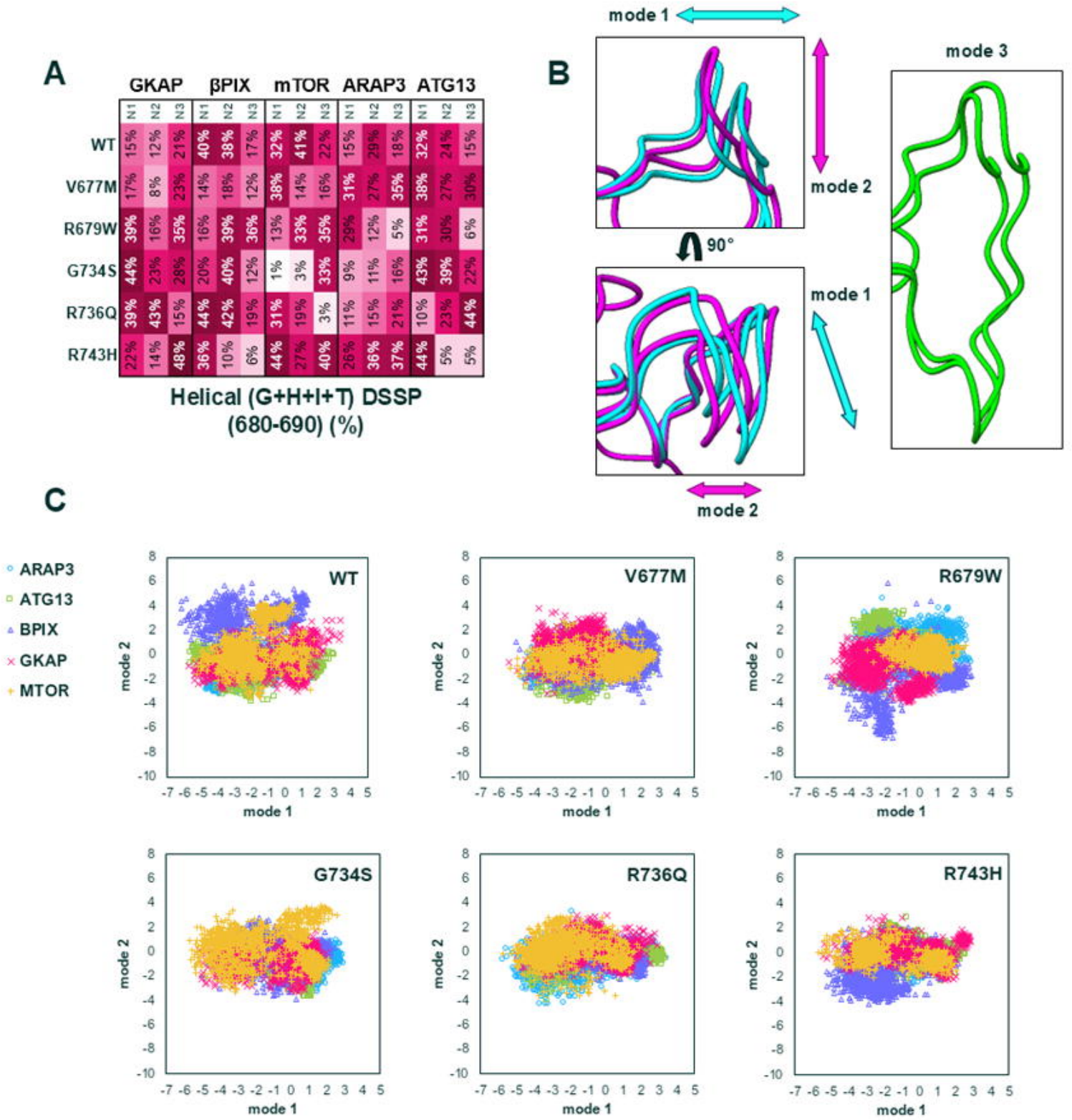
A
GKAP βPIX mTOR ARAP3 ATG13
N1 N2 N3
WT 15% 12% 21% 40% 38% 17% 32% 41% 22% 15% 29% 18% 32% 24% 15%
V677M 17% 8% 23% 14% 18% 12% 38% 14% 16% 31% 27% 35% 38% 27% 30%
R679W 39% 16% 35% 16% 39% 36% 13% 33% 35% 29% 12% 5% 31% 30% 6%
G734S 44% 23% 28% 20% 40% 12% 1% 3% 33% 9% 11% 16% 43% 39% 22%
R736Q 39% 43% 15% 44% 42% 19% 31% 19% 3% 11% 15% 21% 10% 23% 44%
R743H 22% 14% 48% 36% 10% 6% 44% 27% 40% 26% 36% 37% 44% 5% 5%
Helical (G+H+I+T) DSSP
(680-690) (%)
B
mode 1
mode 2
mode 3
90°
mode 1
mode 2
C
ARAP3
ATG13
BPIX
GKAP
MTOR
WT
V677M
R679W
G734S
R736Q
R743H
mode 1
mode 2

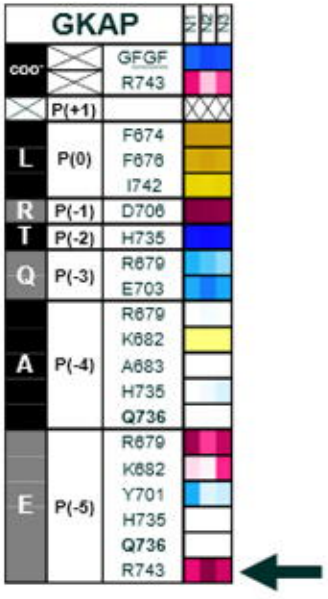

R736Q:GKAP

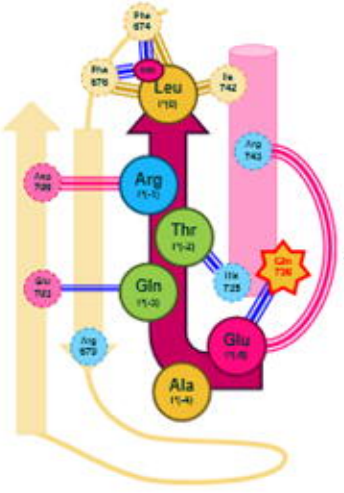

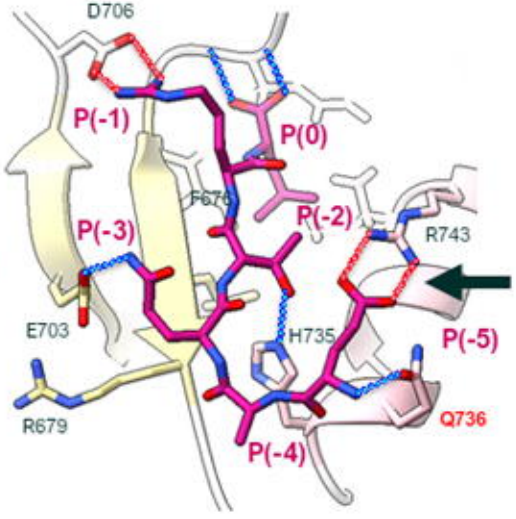

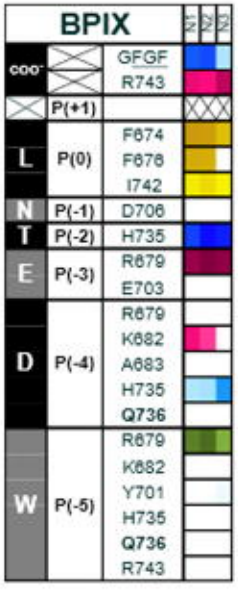

R736Q:βPIX

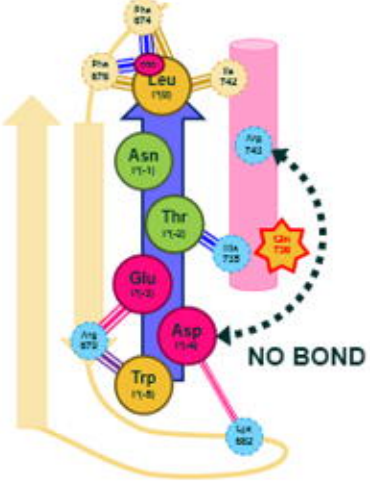

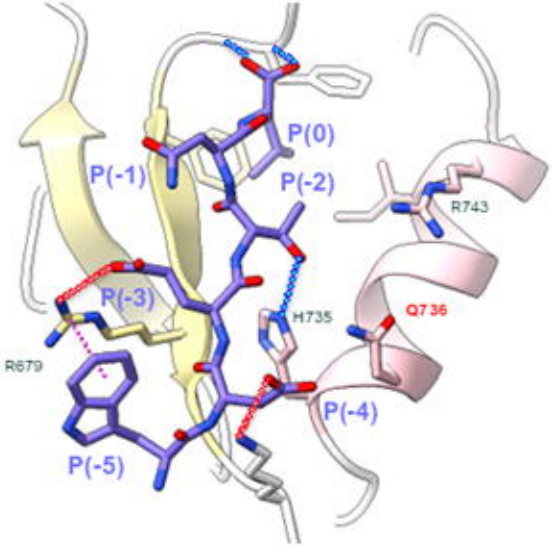

A

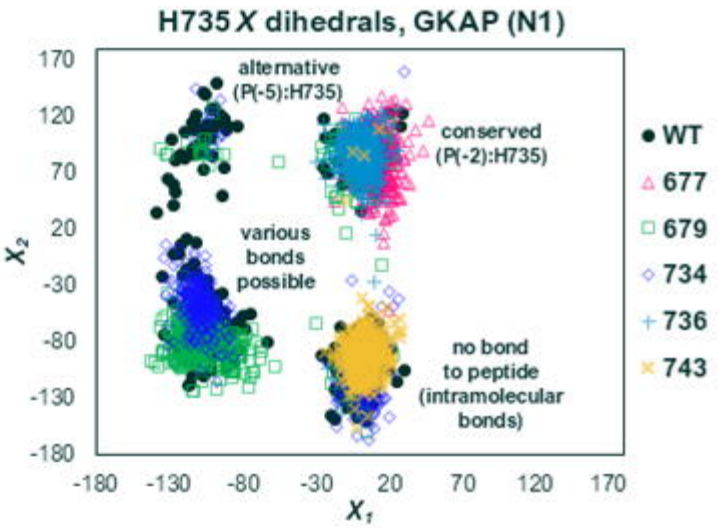

B

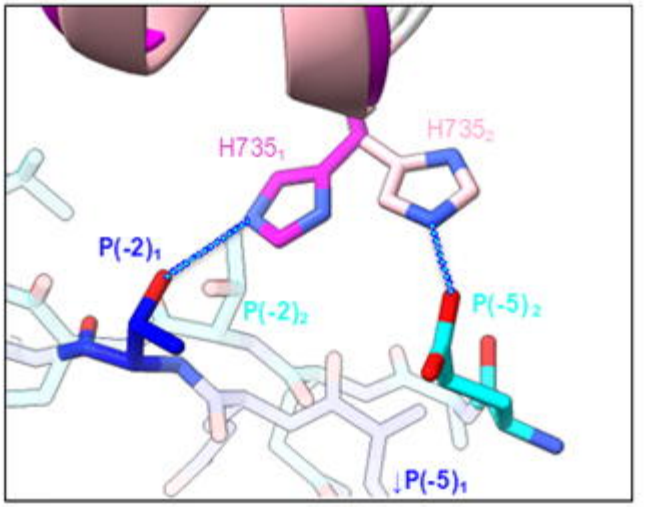

C

	GKAP			βPIX			mTOR			ARAP3			ATG13		
	N1	N2	N3	N1	N2	N3	N1	N2	N3	N1	N2	N3	N1	N2	N3
WT	21%	12%	56%	87%	93%	70%	18%	66%	7%	71%	81%	76%	42%	85%	72%
V677M	83%	45%	91%	47%	94%	83%	63%	67%	56%	75%	24%	47%	90%	91%	80%
R679W	31%	26%	64%	17%	7%	6%	49%	67%	73%	8%	1%	2%	3%	1%	3%
G734S	6%	40%	23%	81%	5%	91%	85%	50%	57%	84%	27%	83%	80%	80%	8%
R736Q	94%	96%	94%	61%	87%	79%	84%	45%	72%	45%	53%	40%	43%	74%	80%
R743H	1%	91%	0%	63%	50%	77%	92%	87%	44%	81%	36%	60%	91%	51%	28%

H735(Nε/Nδ)-P(-2)(OH) H-bond (%)